Improved micro-continuum approach for capillary-dominated multiphase flow with reduced spurious velocity

Cite as: Physics of Fluids (in press) (2022); https://doi.org/10.1063/5.0127603
Submitted: 22 September 2022 • Accepted: 21 November 2022 • Accepted Manuscript Online: 21 November 2022

Zhiying Liu, Junyu Yang, Qianghui Xu, et al.

Improved micro-continuum approach for capillary-dominated multiphase flow with reduced spurious velocity

Zhiying Liu (刘志颖),[1,2] Junyu Yang (杨君宇),[1,2] Qianghui Xu (许强辉),[1,2,3,a)] and Lin Shi (史琳)[1,2]

[1]Key Laboratory for Thermal Science and Power Engineering of the Ministry of Education, Department of Energy and Power Engineering, Tsinghua University, Beijing 100084, China.

[2]Key Laboratory for CO_2 Utilization and Reduction Technology of Beijing, Beijing 100084, China.

[3]School of Mechanical Engineering, Beijing Institute of Technology, Beijing 100081, China.

Corresponding author: a) xuqh12@tsinghua.org.cn

KEYWORDS

Micro-continuum; Multiscale porous media; Multiphase flow; Spurious velocity; Volume of fluid

ABSTRACT

A diverse range of multiphase flow and transport occurs in multiscale porous media. The multiphase micro-continuum Darcy–Brinkmann–Stokes (DBS) model has been developed to simulate the multiphase flow at both the pore and continuum scales via single-field equations. However, the unacceptable spurious velocities produced by the conventional micro-continuum DBS model present challenges to the modeling of capillary-dominated flow dynamics. This study improves the micro-continuum DBS model to mitigate these spurious velocities at the gas–liquid interface and contact-line regions. A hybrid interpolation scheme is proposed to improve the computational accuracy of the interface curvature and reduce the spurious velocity around the gas–liquid interface by 1–2 orders of magnitude. At the porous boundary, the normal to the gas–liquid interface is corrected, and the normal to the solid–fluid interface is smoothed to guarantee the prescribed wettability condition and decrease the spurious velocities at the contact-line region by an order of magnitude. A series of static and dynamic benchmark cases are investigated to demonstrate that the improved DBS model can simulate capillary-dominated multiphase flows with negligible spurious velocities at capillary numbers as low as 10^{-4} in both simple and complex geometries. The improved DBS model can combine X-ray computed micro-tomography images to perform multiscale simulations of capillary-dominated multiphase flow and understand the effect of sub-resolution porosity on fluid dynamics in naturally multiscale rocks.

I. INTRODUCTION

Multiphase flows within complicated porous media are widely encountered in many natural and engineering systems, including CO_2 geological sequestration,[1] hydrocarbon recovery,[2, 3] and electrochemical energy systems.[4-7] In these scenarios, multiphase flow and transport are complex phenomena, involving strong coupling among inertial, viscous, and interfacial forces in natural geological structures.[8] In the bulk-fluid phases, such as gas and liquid phases, two immiscible fluids are separated by an interface, and the interfacial tension strongly influences the shape, movement, and evolution of the phase interface. The viscous force acts tangentially to impede the relative phase motion. In the bulk fluid phases, such as gas and liquid, two immiscible fluids are separated by an interface, where the interfacial tension strongly influences the shape to minimize the interfacial energy. When a fluid of higher density and lower viscosity displaces another fluid of lower density and higher viscosity, the flow process is intrinsically unstable, leading to the fingering of phase interfaces. The porous medium contains considerable fluid-solid interfaces. A contact-line region emerges when the gas-liquid interface joins a solid surface, where the wall-adhesion force governs the contact angle and the contact line dynamics [9]. In the low-capillary flow regime, the gas-liquid interfacial force and the wall-adhesion force significantly control the phase evolution and distribution in heterogeneous porous media. A deep understanding of the multiphase fluid dynamics is fundamental for predicting accurate gas, water, or oil fluxes through geological structures and determining the techno-economic feasibility of subsurface engineering techniques.

Natural geological structures are typically heterogeneous, multiscale assemblies.[10] Although the porous domain of interest is limited to the millimeter or centimeter scale, the pore space can have length scales covering several orders of magnitude,[11] from micrometer-range pores ($\sim O(10)\ \mu\text{m}$) to sub-micrometer-range pores ($\sim O(100)\ \text{nm}$). Multiscale porous structures can be imaged using various imaging modalities, such as X-ray computed micro-tomography (micro-CT), which commonly offers a resolution of a few microns per voxel.[11] With such micrometer-scale resolution, the micrometer-range pores can be resolved to illustrate the void space and the surrounding solid boundary clearly. In contrast, the sub-micrometer-range pores are hidden below the image resolution.[11] The sub-voxel porosity of the unresolved porous medium can be estimated based on the gray intensity, leading to the unresolved porous medium being represented by the effective continuum.[12, 13] The varying representation of porous media at two scales cannot explicitly characterize the connectivity of the resolved and unresolved pore space, increasing the difficulty of modeling the multiphase fluid dynamics.[10, 11, 14] Accordingly, two independent mathematical and numerical models are required to adapt the scale-dependent representations of the porous media and account for different multiphase flow physics. The inertial and viscous forces may dominate in the

fully resolved pore space,[15] whereas the multiphase flow can be directly simulated using the Navier–Stokes equation, referred to as pore-scale modeling, in which the gas–liquid interface is explicitly tracked or captured, and the interface tension force is calculated based on the Young–Laplace law.[16] The capillary force and porous drag force gradually become dominant over the viscous dissipative term within the sub-micrometer-range pores, the result of reduced fluid velocity and intensified solid–fluid friction.[17] Correspondingly, the flow is usually modeled by the multiphase Darcy's law in the unresolved pore medium, referred to as continuum-scale modeling.[14, 16, 18] Different from the direct simulation of the inertial, viscous, and interfacial forces in pore-scale modeling, continuum-scale modeling prescribes the porosity-dependent and saturation-dependent transport properties of the porous representative elementary volume, including the relative permeability and capillary pressure, to describe the nonlinear relation between the phase-averaging velocity and the driving force.[16, 19-21] Notably, the resolved porous medium coexists with the unresolved porous medium, making it necessary to consider their interaction via appropriate boundary conditions. Therefore, predictive modeling of multiphase flow physics through the inherently multiscale porous medium is highly challenging.

Hybrid-scale modeling is an elegant idea for modeling multiscale flow and transport.[22-29] In this approach, single-field equations are introduced to provide a unified framework for describing the scale-dependent physics across the multiscale porous media. This idea dates back to the work of Brinkmann,[30] who proposed the single-phase Darcy–Brinkmann–Stokes (DBS) momentum equation. TABLE I lists a brief summary of development and application of the micro-continuum DBS model. In the case of single-phase flow, combining the Brinkmann term with Darcy's law means that the DBS equation remains valid for both the large-scale channel and the porous domain.[17, 22] Soulaine et al.[14, 18] developed the micro-continuum DBS framework for pore-resolved simulations of single-phase flow. The cornerstone of the micro-continuum framework is the local porosity field ε, which enables adaptation to the multiscale structure. A bounding value of ε=1 represents the resolved macropores, while a bounding value of $\varepsilon = 0 \equiv 0.01$ characterizes the impermeable solid,[31] and the intermediate range $0 < \varepsilon < 1$ describes the unresolved pores. Relying on volume-averaging theory,[32] the DBS equation solves the standard Navier–Stokes flow in the resolved macropore channels, tends asymptotically to Darcy's law in the unresolved porous medium, and reproduces the nonslip velocity condition at the macropore–rock interface by penalization.[15, 16] Many numerical studies have leveraged the micro-continuum DBS framework to demonstrate its reliability in modeling single-phase flows across multiscale porous media.[12, 31, 33-35] Scheibe et al.[33] used the DBS equation to simulate flow and transport in 3D micro-CT images with unresolved pores, achieving improved agreement with experimental results. For simulations of reactive flows across a multiscale porous medium, another appealing advantage of the micro-continuum framework lies in its ability to handle the dynamic evolution of the solid–fluid interface without requiring a re-

meshing strategy. For example, the mineral dissolution of a single calcite crystal was simulated by Soulaine et al.,[34] and their results agreed with the classic arbitrary Lagrangian–Eulerian solver. Maes et al. improved the formulations to localize the reaction at the fluid-solid interface more accurately. They found the micro-continuum DBS framework is significantly faster than the Arbitrary Lagrangian Eulerian (ALE) method for simulations of calcite dissolutions, since the ALE method requires additional treatment for interface displacement.[36] Ashrafizadeh et al. solved the Stokes-Brinkman and the Poisson-Nernst_Planck equations simultaneously to explore the effect of nanochannel shape on the ion transfer behavior.[37, 38] Xu et al.[31] extended the pore-scale micro-continuum model to non-isothermal reactive flow through a multiscale porous medium. They demonstrated the model improvement in terms of mass and energy conservation compared with the previous lattice Boltzmann methods. Therefore, single-phase fluid dynamics modeling across the multiscale porous medium is well established within the micro-continuum framework, and is widely used in simulations of reactive flow in fractures and mineral precipitation.[35, 39-42]

The multiphase micro-continuum DBS framework has recently modeled multiphase flows in a multiscale porous medium. Horgue et al.[43] and Soulaine et al.[14, 18] proposed two-phase micro-continuum DBS frameworks by developing a multiphase DBS equation to describe the two-phase flow at both the pore and continuum scales. The DBS multiphase model was reduced to the classic volume-of-fluid (VOF) method in the resolved macropores and tended towards the multiphase Darcy model in the unresolved porous regions. Nonetheless, the gravity and capillary effects were not accounted for within the unresolved porous domain. Carrilo et al.[16] later proposed an improved multiphase micro-continuum model with a theoretical derivation rooted in elementary physics and volume-averaging principles. The critical feature of this improved multiphase micro-continuum model is its rigorous derivation of multiscale parameters, including the relative velocity $\boldsymbol{v}_r$, drag force coefficient μk^{-1}, and capillary force $\boldsymbol{F}_c$, which complement the sub-grid relative permeability, gravity, and capillary effects. The physical meaning and mathematical formulation of these multiscale parameters differs in the resolved and unresolved porous media, allowing the improved DBS multiphase model to asymptotically match the scale-dependent multiphase model, i.e., the VOF model at the pore scale and the multiphase Darcy's law at the continuum scale. The theoretically sound micro-continuum model was verified using numerical cases consisting of continuum-scale, pore-scale, and hybrid-scale multiphase flows.[16]

TABLE I. A summary of the development and application of the micro-continuum model.

Year	Authors	Equations	Fluid	Remarks	Reference
1949	Brinkman	Darcy-Brinkman (DB)	single phase	presented the DB equation for single-phase flow on a dense swarm of particles.	[30]

1967	Beavers et al.	Darcy-Brinkman (DB)	single phase	established Beavers-Joseph boundary conditions to simultaneously solve flow through porous and solid-free regions.	[28]
1990	Hsu and Cheng	Darcy-Brinkman-Stokes (DBS)	single phase	volume averaged the Navier-Stokes equations in a control volume containing fluids and solids.	[29]
2002	Golfier et al.	Stationary Darcy-Brinkman (DB)	single phase	simulated dissolution of porous media and characterized the influence of flow parameters on the wormhole development	[24]
2014	Horgue	Darcy-Brinkman-Stokes (DBS)	single phase	realized a complete workflow from pore-scale imaging to absolute permeability computation using the single-phase DBS model	[43]
2016	Soulaine et al.	Darcy-Brinkman-Stokes (DBS)	single phase	employed micro-continuum approach to model the flow, transport, and dissolution in fractured media	[15]
2018	Soulaine et al	Darcy-Brinkman-Stokes (DBS)	multiphase	proposed a micro-continuum approach to simulate the dissolution of minerals at the pore scale in the presence of multiple fluid phases	[18]
2020	Carrilo et al.	Darcy-Brinkman-Stokes (DBS)	single phase	derived, implemented, tested, and verified a multiscale model for two-phase flow in porous media.	[16]
2021	Xupeng He et al.	Darcy-Brinkman-Stokes (DBS)	single phase	simulated matrix-fracture interaction and fluid leakage using the single-phase DBS model.	[41]
2022	Hang Deng et al.	Darcy-Brinkman-Stokes (DBS)	single phase	performed simulations of dissolution-precipitation systems using the single-phase DBS model.	[42]
2022	Carrilo et al.	Darcy-Brinkman-Stokes (DBS)	multiphase	studied the influence of flow within the sub-resolution porosity on multiphase flow in heterogeneous porous media.	[39]

Several limitations in the multiphase micro-continuum model persist. First, the application of the current model is limited to multiphase drainage and imbibition with high capillary numbers of $\mathrm{Ca} = \mu u / \sigma = 10^{-1}$ to 10^{-2},[16] where μ is the characteristic dynamic viscosity, u is the inlet velocity, and σ is the interfacial tension. In this situation, the viscous force dominates the interfacial dynamics over the capillary force. However, for natural subsurface transport problems, the capillary forces are more significant, generally resulting in capillary numbers of 10^{-4} or less.[9, 44] At low capillary numbers, spurious currents often appear near the gas–liquid interface and the three-phase contact-line region.[45] If the interface tension model is not handled carefully, these spurious currents could become larger than the physical flow, leading to unphysical fluid dynamics.[9, 44] Therefore, the predictive capacity of the multiphase micro-continuum model in a multiscale porous medium must be evaluated and improved at low capillary numbers. Second, similar to the top-down definition of the contact angle in the classic VOF approach, the multiphase micro-continuum model treats the contact angle θ as an upscaled parameter, depending on the sub-grid-scale information.[16] The current model inherits the correction strategy of the VOF approach to guarantee the interface on the porous boundary has a prescribed contact angle θ.[16, 18, 43] Accordingly, the contact angle correction is achieved by replacing the calculated normal to the gas–liquid interface $\boldsymbol{n}_{\mathrm{lg}}$ with the locally modified norm $\tilde{\boldsymbol{n}}_{\mathrm{lg}}$ to satisfy the wettability condition $\tilde{\boldsymbol{n}}_{\mathrm{lg}} = \cos\theta \boldsymbol{n}_{\mathrm{p}} + \sin\theta \boldsymbol{t}_{\mathrm{p}}$, where $\boldsymbol{n}_{\mathrm{p}}$ and $\boldsymbol{t}_{\mathrm{p}}$ are the normal and tangent vectors to the porous boundary, respectively. As opposed to the standard boundary condition (a solid wall once rock-occupied cells have been removed from the mesh) in the VOF approach (see FIG. 1), liquid-statured or gas-saturated porous regions impact the saturation gradient $\nabla\alpha_{\mathrm{l}}$ at the porous boundary. This results in an unintended normal to the gas–fluid interface of $\boldsymbol{n}_{\mathrm{lg}} = \nabla\alpha_{\mathrm{l}} / \|\nabla\alpha_{\mathrm{l}}\|$. As such, the corrected contact angle arising from the abnormal $\boldsymbol{n}_{\mathrm{lg}}$ significantly deviates from the imposed contact angle in the capillary rise case studied by Carrilo et al.[16] Third, the smoothed normal vector to the porous boundary $\boldsymbol{n}_{\mathrm{wall}}$ is essential for alleviating the spurious velocity near the contact-line region. In the classic VOF approach, an unstructured mesh is used to match the solid boundary and smooth the solid wall-normal vector.[46, 47] In contrast, the micro-continuum model uses structured Cartesian grids, with a staircase mesh used to approximate the porous boundary.[16, 31] The resulting normal vector to the porous boundary $\boldsymbol{n}_{\mathrm{p}}$ does not provide smoothing, particularly at sharp corners. Therefore, the smoothing scheme of the normal vector to the porous boundary should be investigated to achieve the stable simulation of

multiphase flow across a multiscale porous medium at low capillary numbers.

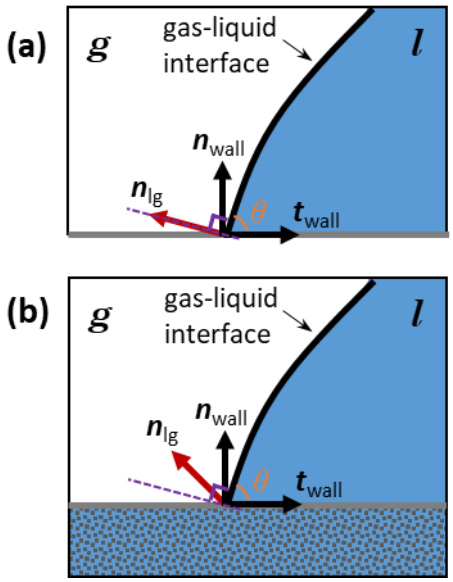

FIG. 1. Schematic representation of contact angle correction: (a) VOF approach, (b) multiphase micro-continuum approach. The red solid arrow represents the calculated normal to the gas–liquid interface $\boldsymbol{n}_{lg}$ and the purple dotted line represents the correct direction of $\boldsymbol{n}_{lg}$.

This paper improves the multiphase micro-continuum DBS model to achieve stable simulations of the two-phase flow at capillary numbers as small as 10^{-4}. Particular attention is paid to spurious velocities at the gas–liquid interface and contact-line region. First, we demonstrate how different unit normal vectors to the gas–liquid interface impact the interface curvature and spurious currents. Accordingly, a new formulation of the unit normal vector to the gas–liquid interface is proposed. This formulation reduces the spurious velocities by at least one order of magnitude compared with that of the *interFoam* model (the standard VOF-based solver in OpenFOAM). Second, a saturation extrapolation algorithm is devised to reconstruct the saturation gradient near the porous boundary, such that the correction strategy in the VOF approach can accurately enforce the expected contact angle. Third, regarding the porous surface represented by a staircase approximation, a weighted scheme for smoothing the normal to the porous boundary is developed to eliminate the spurious currents near the contact-line region. Finally, the developed model is verified by various test cases in which the results are compared with those obtained analytically or from the *interFoam* solver. The test cases include a stationary gas bubble, droplets on flat and curved surfaces, capillary rise, and liquid drainage in complex porous media.

The remainder of this paper is organized as follows. In Section II, mathematical models for the multiphase micro-continuum DBS framework are introduced. Section III describes the improved numerical models, equation discretization, and solver workflow based on the OpenFOAM open-source simulation platform. In Section IV, a series of validation cases for the multiphase flow are

presented. Finally, Section V summarizes the conclusions to this study.

II. MATHEMATICAL MODELS

The two-phase micro-continuum framework consists of partial differential equations, which are averaged over control volumes to govern the conservation of mass, momentum, and fluid saturation, and can be solved for the single-field variables $\bar{\boldsymbol{v}}$, p, and α_l. In image-based simulations, the control volumes correspond to the image voxels, which can contain one or two fluid phases (V_l / V_g), a solid phase (V_s), or fluid/solid aggregates. Concerning the content within each control volume, the averaged single-field variables are closely related to the local porosity field ε_f and the saturation field α_l, which are defined as

$$\varepsilon_f = \frac{(V_l + V_g)}{V}, \tag{1}$$

$$\alpha_l = \frac{V_l}{V_l + V_g}. \tag{2}$$

The local porosity field is used to describe multiscale pore structure, consisting of resolved macropores ($\varepsilon = 1$),unresolved porous regions ($0 < \varepsilon < 1$), and impermeable solid regions ($\varepsilon \approx 0$). The saturation field is defined as the ratio of the liquid volume over the total fluid phase volume within each control volume. According to the local porosity field and the saturation field, the single-field variables are defined throughout the computational domain as

$$\bar{p} = \alpha_l \bar{p}_l^l + \alpha_g \bar{p}_g^g, \tag{3}$$

$$\bar{\boldsymbol{v}} = \varepsilon(\alpha_l \bar{\boldsymbol{v}}_l^l + \alpha_g \bar{\boldsymbol{v}}_g^g). \tag{4}$$

Here, $\bar{p}$ is the averaged pressure over the control volume, while $\bar{p}_i^i$ (i=l, g) denotes the averaged pressure over the phase. The same notation is applied to the velocity $\boldsymbol{v}$. Assuming the fluid phases to be incompressible, isothermal, and immiscible, the single-field continuity equation, saturation equation, and momentum equation in the multiphase micro-continuum DBS framework can be written as[16]

$$\nabla \cdot \bar{\boldsymbol{v}} = 0, \tag{5}$$

$$\frac{\partial \varepsilon \alpha_l}{\partial t} + \nabla \cdot \left(\alpha_l \bar{\boldsymbol{v}}\right) + \nabla \cdot \left(\varepsilon \alpha_l \alpha_g \bar{\boldsymbol{v}}_r\right) = 0, \tag{6}$$

$$\frac{1}{\varepsilon}\left(\frac{\partial \rho \bar{\boldsymbol{v}}}{\partial t} + \nabla \cdot \left(\frac{\rho}{\varepsilon}\bar{\boldsymbol{v}}\bar{\boldsymbol{v}}\right)\right) = -\nabla \bar{p} + \rho \mathbf{g} + \nabla \cdot \left(\mu\left(\nabla \bar{\boldsymbol{v}} + \nabla \bar{\boldsymbol{v}}^T\right)\right) - \mu k^{-1} \bar{\boldsymbol{v}} + \boldsymbol{F}_c. \tag{7}$$

In Eq. (7), the last term represents the surface tension forces, while the second-to-last term is the drag force, describing the porous resistance exerted on the pore walls. The governing equations above hold for the entire domain, regardless of the phases occupying the cells. In the resolved

macropore regions, the multiphase micro-continuum model matches the standard VOF-based Navier–Stokes equation, and so the saturation field delineates the liquid phase ($\alpha_l = 1$),gas phase ($\alpha_l = 0$), and the gas–liquid interface ($0 < \alpha_l < 0$). In contrast, the multiphase micro-continuum model tends asymptotically to the two-phase Darcy equation, in which the saturation field represents the actual liquid saturation. The scale-dependent behavior of the micro-continuum model is achieved by a set of multiscale parameters $\bar{\boldsymbol{v}}_r, \rho, \mu k^{-1}$, and $\boldsymbol{F}_c$, which are derived through volume averaging and asymptotic matching principles.[16]

The relative velocity $\bar{\boldsymbol{v}}_r$ is given by[16]

$$\bar{\boldsymbol{v}}_r = \begin{cases} C_\alpha \max(|\bar{\boldsymbol{v}}|)\dfrac{\nabla\alpha_l}{|\nabla\alpha_l|}, & \text{in macropore regions} \\ \varepsilon^{-1}\left[\begin{array}{c} -\left(\dfrac{M_l}{\alpha_l}-\dfrac{M_g}{\alpha_g}\right)\nabla\bar{p}+\left(\dfrac{\rho_l M_l}{\alpha_l}-\dfrac{\rho_g M_g}{\alpha_g}\right)\mathbf{g} \\ +\left(\dfrac{M_l\alpha_g}{\alpha_l}+\dfrac{M_g\alpha_l}{\alpha_g}\right)\nabla p_c-\left(\dfrac{M_l}{\alpha_l}-\dfrac{M_g}{\alpha_g}\right)p_c\nabla\alpha_l \end{array}\right], & \text{in porous regions} \end{cases} \tag{8}$$

where C_α is the interface compression coefficient, which is empirically determined as a value between 0 and 4. $M_i = k_0 k_{r,i} / \mu_i$ (i = l,g) is the mobility of fluid phase i, where k_0 is the absolute permeability of the porous medium and $k_{r,i}$ is the relative permeability of fluid phase i. In the macropore regions, the relative velocity is given by the classic VOF approach, which is active at the gas–liquid interface to sharpen the interface in the normal direction $\boldsymbol{n}_{lg} = \dfrac{\nabla\alpha_l}{|\nabla\alpha_l|}$ with an amplitude based on the maximum single-field velocity. In the porous regions, the formulation of the relative velocity can be derived by matching the formulation of the micro-continuum model to the two-phase Darcy model. Notably, the relative velocity in the porous regions is related to the phase mobility M_i, gravitational acceleration $\mathbf{g}$, and macroscopic capillary pressure p_c. As a result, the relative velocity can account for the comprehensive interplay of the relative permeability, gravity, and capillary effects. Conventionally, the relative permeability $k_{r,i}$ and the macroscopic capillary pressure p_c are represented as functions of saturation to complement the sub-grid hydrodynamic impact of the porous micro-structure at the continuum scale. Relative permeability models, such as the Brooks and Corey model,[20] and capillary pressure models, such as the Van Genutchen model,[19] are summarized in the literature.[16]

The formulation of the capillary force $\boldsymbol{F}_c$ significantly differs from the content of the grid cell, as shown by Eq. (9). In the macropore regions, the capillary force emerges at the curved phase interface to balance the pressure gradient. Here, the well-known continuum surface force (CSF) formulation is adopted to quantify the capillary force.[48] The CSF model assumes the surface tension to be constant within each control volume, and then approximates the volume-averaged surface

tension force in terms of the mean interface curvature. The mean interface curvature $\bar{\kappa} = \nabla \cdot \left(\boldsymbol{n}_{\mathrm{lg}} \right)$ is estimated from the normal to the gas–liquid interface, $\boldsymbol{n}_{\mathrm{lg}}$. Note that some variants of the CSF model, such as the sharp surface force (SSF) model, mitigate the magnitude of spurious currents at the gas–liquid interface.[9, 46] However, our numerical experiments found that, although the SSF model can work well in some simple structures, such as stationary gas bubbles, alleviating the spurious velocities becomes practically ineffective in complex porous media with significant contact-line regions. For this reason, the SSF model is not applied in this work. Instead, numerical approaches for the micro-continuum framework are introduced in Section III to effectively suppress the spurious currents in the porous medium based on the CSF model. Similar to the relative velocity $\bar{\boldsymbol{v}}_{\mathrm{r}}$, the capillary force in the porous regions can be determined from the two-phase Darcy model.

$$\boldsymbol{F}_{\mathrm{c}} = \begin{cases} -\varepsilon^{-1}\sigma\nabla\cdot\left(\boldsymbol{n}_{\mathrm{lg}}\right)\nabla\alpha_{\mathrm{l}}, & \text{in macropore regions} \\ \left[M^{-1}\left(M_{\mathrm{l}}\alpha_{\mathrm{g}} - M_{\mathrm{g}}\alpha_{\mathrm{l}}\right)\left(\dfrac{\partial p_{\mathrm{c}}}{\partial \alpha_{\mathrm{l}}}\right) - p_{\mathrm{c}} \right]\nabla\alpha_{\mathrm{l}}, & \text{in porous regions} \end{cases} \tag{9}$$

The drag force coefficient quantifies the relation between the fluid–solid friction and the single-field velocity. In the porous regions, the drag force coefficient is defined by a harmonic average of the gas and liquid phase mobility, as given by Eq. (10); in the macropore regions, it vanishes to zero. Unlike the artificial modification of the drag force term with respect to the solid content in grid cells, the dissipative viscous term is retained in the DBS momentum model. However, the relative magnitude between the porous drag force term and the dissipative viscous term naturally varies from the make-up of the grid cells. The porous drag force term gradually becomes dominant over the dissipative viscous term with $0 < \varepsilon < 1$.[15, 49] This gradual transition ensures the continuity of the stress and velocity in the entire computational domain.[22] Eventually, together with the scale-separated definition of the capillary force in Eq. (9) and the fluid density in Eq. (11), the micro-continuum model reduces to the two-phase Darcy solution for the description of the continuum-scale multiphase flow in the porous regions and to the VOF approach for explicitly tracking the gas–liquid interface and three-phase contact lines in the macropore regions.[16]

$$\mu k^{-1} = \begin{cases} 0, & \text{in macropore regions} \\ k_0^{-1}\left(\dfrac{k_{\mathrm{r,l}}}{\mu_{\mathrm{l}}} + \dfrac{k_{\mathrm{r,g}}}{\mu_{\mathrm{g}}} \right)^{-1}, & \text{in porous regions} \end{cases} \tag{10}$$

$$\rho = \begin{cases} \rho_{\mathrm{l}}\alpha_{\mathrm{l}} + \rho_{\mathrm{g}}\alpha_{\mathrm{g}}, & \text{in macropore regions} \\ \left(\rho_{\mathrm{l}}M_{\mathrm{l}} + \rho_{\mathrm{g}}M_{\mathrm{g}}\right)M^{-1}, & \text{in porous regions} \end{cases} \tag{11}$$

Similar to the solid wall, the porous boundary between the macropore and porous regions produces wall adhesion forces due to uneven molecular forces along the contact lines. Theoretically,

the macroscopic contact angle at the porous boundary is related to various sub-grid interface properties, such as the fluid interfacial tension, porous microstructure, and spreading film shape.[50] However, this study treats the contact angle as an upscaled parameter and only considers the macroscopic contact-line dynamics. Therefore, the normal to the gas–liquid interface at the porous boundary is modified according to Eq. (12) to ensure that the contact angle is equal to the prescribed value of θ:

$$\tilde{\boldsymbol{n}}_{\mathrm{lg}} = \cos\theta \boldsymbol{n}_{\mathrm{p}} + \sin\theta \boldsymbol{t}_{\mathrm{p}}, \tag{12}$$

where $\boldsymbol{n}_{\mathrm{p}}$ and $\boldsymbol{t}_{\mathrm{p}}$ are the normal and tangent vectors to the porous boundary, respectively. According to Horgue et al.[43] and Soulaine et al.,[18] Eq. (12) can be recast into the formulation of Eq. (13) for convenient computation:

$$\tilde{\boldsymbol{n}}_{\mathrm{lg}} = \frac{\cos\theta - \cos\theta_{\mathrm{I}}\cos(\theta_{\mathrm{I}} - \theta)}{1-\cos^2\theta_{\mathrm{I}}}\boldsymbol{n}_{\mathrm{p}} + \frac{\cos(\theta_{\mathrm{I}} - \theta) - \cos\theta_{\mathrm{I}}\cos\theta}{1-\cos^2\theta_{\mathrm{I}}}\boldsymbol{n}_{\mathrm{lg}}, \tag{13}$$

where $\theta_{\mathrm{I}} = \cos^{-1}(\boldsymbol{n}_{\mathrm{p}} \cdot \boldsymbol{n}_{\mathrm{lg}})$ and $\boldsymbol{n}_{\mathrm{lg}}$ is the normal to the gas–liquid interface yielded by the current saturation field. These values may not satisfy the targeted wettability condition and should be corrected to θ and $\tilde{\boldsymbol{n}}_{\mathrm{lg}}$, respectively.

In conclusion, Eq. (7) constitute the governing equations, and Eq. (9) closure the equations by defining the relative velocity $\bar{\boldsymbol{v}}_{\mathrm{r}}$, the drag force μk^{-1}, and the surface tension force $\boldsymbol{F}_{\mathrm{c}}$, in both macropore and porous regions . Eq. (13) is used to correct the calculated contact angle to the prescribed value.

III. NUMERICAL METHODS

The finite volume method (FVM) is used to solve the mathematical model, where the partial differential equations are first discretized by integrating them over each control volume to yield a set of algebraic equations. To achieve an acceptable magnitude for the spurious velocities at capillary numbers as low as 10^{-4}, particular attention is paid to the discretization of the capillary force at the gas–liquid interface and the contact-line region. A hybrid formulation of the unit normal vector to the gas–liquid interface is proposed to enable accurate computations of the interface curvature. Concerning the multiscale nature of the micro-continuum framework, the saturation extrapolation algorithm is introduced to correct the normal to the gas–liquid interface at the porous boundary. Combined with an improved smoothing scheme of the normal to the staircase-like porous interface, the prescribed contact angle and the reduced spurious velocity can be achieved at the contact-line region. Finally, essential information on the equation discretization and solver

workflow is introduced.

A. Discretization of the normal to the gas–liquid interface

In the macropore regions, the multiphase micro-continuum DBS model reduces to the classic VOF-based Navier–Stokes equation, where the capillary force is described as a body force by the CSF model in Eq. (9). The inaccurate estimation of the interface curvature in the CSF model is believed to destroy the balance of the interfacial forces and intensify the non-physical spurious currents.[9, 44] According to the volume-averaging derivation, the interface curvature within the control volume is approximated as the mean curvature, which can be obtained by $\bar{\kappa} = -\nabla \cdot \boldsymbol{n}_{\mathrm{lg}}$. Numerically, the semi-discretized form of the interface curvature can be obtained using the Gaussian scheme

$$\bar{\kappa} = -\sum \tfrac{1}{V_{\mathrm{i}}} \boldsymbol{n}_{\mathrm{lg},f} \cdot \boldsymbol{S}_f , \tag{14}$$

where the subscript f denotes the field on face f of the control volume, $\boldsymbol{S}_f$ is the outward pointing face surface vector, and V_{i} is the volume of grid cell i. In the *interFoam* (the VOF-based solver in OpenFOAM) and *hybridPorousInterFoam* (open-source implementation of the multiphase micro-continuum model developed by Carrillo et al.[51]) solvers, the face-centered interface norm $n_{\mathrm{lg},f}$ is calculated by the face-centered saturation gradient divided by its magnitude, i.e.,

$$\boldsymbol{n}_{\mathrm{lg},f} = \frac{\langle \nabla \alpha_{\mathrm{l}} \rangle_{c\to f}}{\left\| \langle \nabla \alpha_{\mathrm{l}} \rangle_{c\to f} \right\|}, \tag{15}$$

where $\langle\ \rangle_{c\to f}$ denotes the interpolation operator from the cell-centered field to the face-centered field. This formulation is based on the interpolated saturation gradient, and is referred to hereafter as the IG scheme. In contrast to the IG scheme, the *poreFoam* (open-source two-phase flow solver developed by Raeini et al.[9] and Shams et al.[44]) and *interGCFoam* (open-source multiphase flow and transport solver developed by Maes et al.[52]) methods adopt a different formulation, referred to hereafter as the IN scheme, which directly interpolates the cell-centered unit normal to the face-centered unit norm as

$$\boldsymbol{n}_{\mathrm{lg}} = \frac{\nabla \alpha}{\|\nabla \alpha\|}, \ \boldsymbol{n}_{\mathrm{lg},f} = \langle \boldsymbol{n}_{\mathrm{lg}} \rangle_{c\to f} . \tag{16}$$

The IG and IN schemes underestimate and overpredict, respectively, the interface curvature in numerical experiments. As illustrated in FIG. 2(a), the underlying reason for the underestimation of curvature by the IG scheme is that the interpolated saturation gradient at the face center favors neighboring cell-centered saturation gradients with larger magnitudes, leading to the interpolated

saturation gradient around the grid cell faces being somewhat similar. According to Eq. (14), the numerical surface integral of unit vectors of these interpolated saturation gradients on the cell faces offsets some of the flux fields from the similar components, resulting in an underestimated curvature. By comparison, the IN scheme in FIG. 2(b) adopts the unit normal to the gas–liquid interface with a magnitude of one to ensure the independent contribution of the neighboring cell-centered unit norms to the interpolated face-centered unit norm. Therefore, the IN scheme does not underestimate the curvature. Nonetheless, some curvature overprediction is produced by the IN scheme. This is thought to come from the inherent error of the numerical method, which uses the mean curvature to represent the local curvature at every point of the gas–liquid interface within the grid cell. In the low-capillary-number regime, where the capillary force becomes dominant, the discrepancies in the interface curvature given by both the IG and IN schemes becomes non-negligible and produces significant spurious velocities at the phase interface.

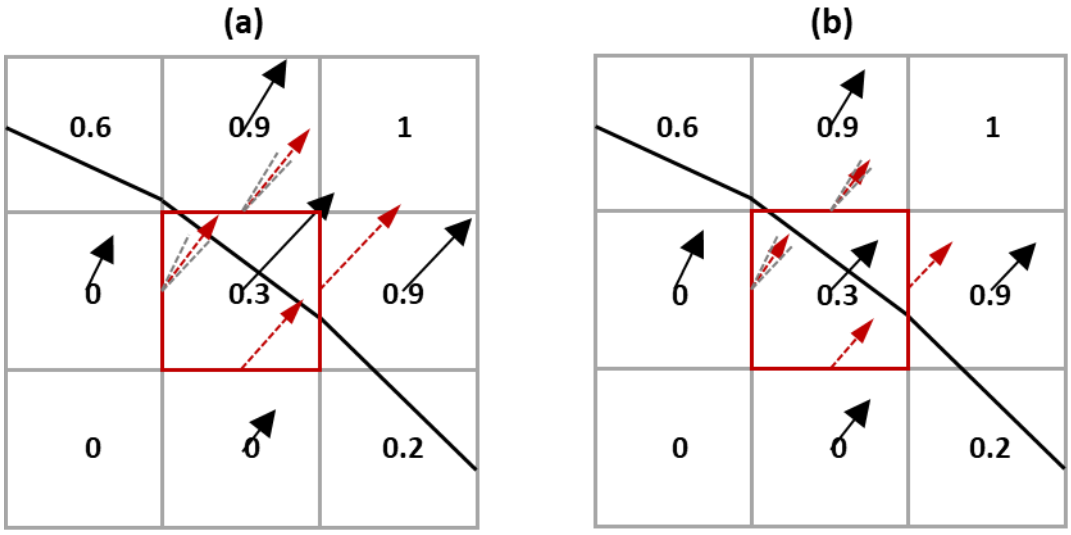

FIG. 2. Graphic representation of cell-centered or face-centered vectors for computing the normal to the gas–liquid interface. (a) Saturation gradients in the IG scheme, (b) normal to the gas–liquid interface in the IN scheme. The black solid arrows represent the cell-centered vectors, while the red dashed arrows depict the face-centered vectors. The gray dashed arrows are formed by moving the cell-centered vectors parallel to the face center for comparison.

For a more accurate computation of the face-centered normal to the gas–liquid interface, a hybrid formulation is proposed in which the counter-impacts of the IG and IN schemes on the interface curvature are neutralized:

$$\boldsymbol{n}_{\mathrm{lg},f} = C_{\mathrm{lg}} \left\langle \frac{\nabla \alpha}{\|\nabla \alpha\|} \right\rangle_{c\to f} + \left(1 - C_{\mathrm{lg}}\right) \frac{\langle \nabla \alpha_1 \rangle_{c\to f}}{\left\| \langle \nabla \alpha_1 \rangle_{c\to f} \right\|} . \tag{17}$$

A value of C_{lg} =0 reduces to the IG scheme, while as C_{lg} approaches 1, the hybrid formulation

reduces to the IN scheme. Because the underprediction by the IG scheme is more serious than the overestimation by the IN scheme, a value of C_{lg} =0.6 is used in the following simulations.

B. Correction of the normal to the gas–liquid interface at the porous boundary

After solving the saturation fields, the obtained normal vector to the gas–liquid interface $\boldsymbol{n}_{lg}$ is used to correct the contact angle at the porous boundary according to Eq. (13). In the micro-continuum framework, the correction strategy for the contact angle is taken from the classic VOF approach.[14, 43] However, different representations of porous media change the direction of the normal vector to the gas–liquid interface at the solid/porous boundary, as shown in FIG. 3. In FIG. 3(a), the VOF approach removes the solid phase from the mesh, and the solid surface is treated as the conventional wall boundary. Accordingly, the normal to the gas–liquid interface is calculated based on the known saturation field within the bulk fluid phase. In contrast, all the grid cells are retained in the micro-continuum framework to describe the multiscale porous medium. They must have nonzero porosity, suggesting that a low-porosity, low-permeability domain will have little void space occupied by the gas or liquid phase. As shown in FIG. 3(b), highly contrasting saturation fields may exist in the solid-free and porous regions, both of which participate in computing the normal to the gas–fluid phase at the porous boundary. As such, the obtained interface norm deviates from its original definition for the contact angle correction algorithm. Furthermore, the nonzero saturation gradient at these porous boundaries introduces a non-physical capillary force and spurious currents. To deal with this problem, the saturation of the solid-free region is extrapolated to the nearby porous region according to Eqs. (18) and (19). As illustrated in FIG. 3(c), the neighboring saturation field at either side of the porous boundary becomes the same to eliminate the component of the saturation gradient pointing from the porous region to the solid-free region. Therefore, the saturation extrapolation algorithm recovers the magnitude and direction of the saturation gradients at the contact-line region to be consistent with the VOF approach. Moreover, the saturation gradient that should not exist along the porous boundary vanishes.

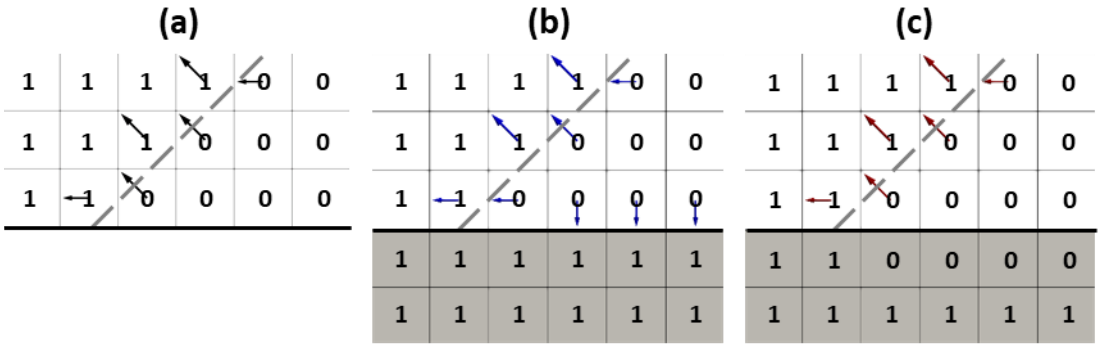

FIG. 3. Graphic representation of the normal to the gas–liquid interface close to the solid/porous boundary: (a) VOF approach, (b) non-corrected normal vectors in the multiphase multiscale model, (c) illustration of the saturation extrapolation from the solid-free region to the porous region and the corrected normal vectors in the multiphase multiscale model. White cells represent the solid-free region, gray cells indicate the porous region, and arrows depict the normal vector to the gas–liquid interface.

$$\chi = \begin{cases} 1, \text{ in the macropore region} \\ 0, \text{ in the porous region} \end{cases}, \quad \chi_f = \text{ceil}\left(\langle \chi \rangle_{c\to f}\right), \tag{18}$$

$$\alpha_{\text{l,corr}} = \begin{cases} \chi\alpha_{\text{l}} + (1-\chi)\dfrac{\left\langle \chi_f \langle \alpha_{\text{l}} \rangle_{c\to f,\text{harmonic}} \right\rangle_{f\to c}}{\left\langle \chi_f \right\rangle_{f\to c}}, & \alpha_{\text{l,solid}} = 1 \\ 1-\left(\chi(1-\alpha_{\text{l}}) + (1-\chi)\dfrac{\left\langle \chi_f \langle 1-\alpha_{\text{l}} \rangle_{c\to f,\text{harmonic}} \right\rangle_{f\to c}}{\left\langle \chi_f \right\rangle_{f\to c}} \right), & \alpha_{\text{l,solid}} = 0 \end{cases} \tag{19}$$

where χ is an indicator function representing whether the grid block belongs to the resolved macropore region or the unresolved porous region. The computation of $\alpha_{\text{l,corr}}$ depends on the occupied phase in the void space of the porous regions, as given by Eq. (19), where $\langle\ \rangle_{f\to c}$ represents interpolation from face center to cell center, while $\langle\ \rangle_{c\to f}$ represents interpolation from cell center to face center. The subscript "harmonic" denotes the harmonic-mean scheme used in the interpolation.

C. Smoothing of the normal to the porous boundary

The normal to the porous boundary is another critical input for the contact angle correction in the contact-line region, as shown by Eq. (13). Concerning the structured Cartesian grid used in the multiphase micro-continuum approach, the normal vectors should be smoothed to represent the complex porous boundaries, which is effective for reducing spurious velocities and improving numerical stability. The *hybridPorousInterFoam* code[16] adopts Eqs. (20)–(24) to smooth the normal to the fluid–solid interface:

$$\boldsymbol{n}_{\text{p},f} = \frac{\nabla \varepsilon_f}{\left\| \nabla \varepsilon_f \right\|}, \tag{20}$$

$$\xi_f = \left\| \boldsymbol{n}_{\text{p},f} \right\|, \tag{21}$$

$$\nabla \varepsilon_{f,\text{i}} = \xi_f \left\langle \left\langle \nabla \varepsilon_{f,\text{i-1}} \right\rangle_{f\to c} \right\rangle_{c\to f}, \text{i} = 1 \sim \text{n} - 1, \tag{22}$$

$$\nabla \varepsilon_{f,\mathrm{n}} = \left\langle \left\langle \nabla \varepsilon_{f,\mathrm{n-1}} \right\rangle_{f \to c} \right\rangle_{c \to f}, \tag{23}$$

$$\tilde{\boldsymbol{n}}_{\mathrm{p},f} = \frac{\nabla \varepsilon_{f,\mathrm{n}}}{\left\| \nabla \varepsilon_{f,\mathrm{n}} \right\|}, \tag{24}$$

where $\nabla \varepsilon_f$ is the face-centered gradient of the local porosity ε, ξ_f is an indicator function representing the porous boundary, and $\boldsymbol{n}_{\mathrm{p},f}$, $\tilde{\boldsymbol{n}}_{\mathrm{p},f}$ are the raw and smoothed unit norms to the porous surface, respectively. The key steps are implemented by Eqs. (22) and (23), which interpolate the gradient of the local porosity from face centers to cell centers and then back to the face centers recursively for i iterations (i≥1). Concerning the smoothing kernel $\left\langle \left\langle \ \right\rangle_{f \to c} \right\rangle_{c \to f}$, which diffuses the smoothed variable away from the porous boundary, the coefficient ξ_f is applied before the kernel in Eq. (22) to limit $\nabla \varepsilon_{f,\mathrm{i}}$ on the porous boundary. Such smoothed normalized norms to the porous boundaries $\tilde{\boldsymbol{n}}_{\mathrm{p},f}$ are illustrated in FIG. 4. The smoothed norms still spread into the vicinity close to the porous boundary due to the absence of a location constraint in Eq. (23). The diffused norms to the porous boundaries $\tilde{\boldsymbol{n}}_{\mathrm{p},f}$ induce the unexpected correction of the normal to the gas–liquid interface $\tilde{\boldsymbol{n}}_{\mathrm{lg}}$ in the vicinity of the porous surface through Eq. (13) and then produce an ill-balanced capillary force in Eq. (9). Finally, spurious velocities are intensified by these smoothed norms to the porous boundary in the contact-line region.

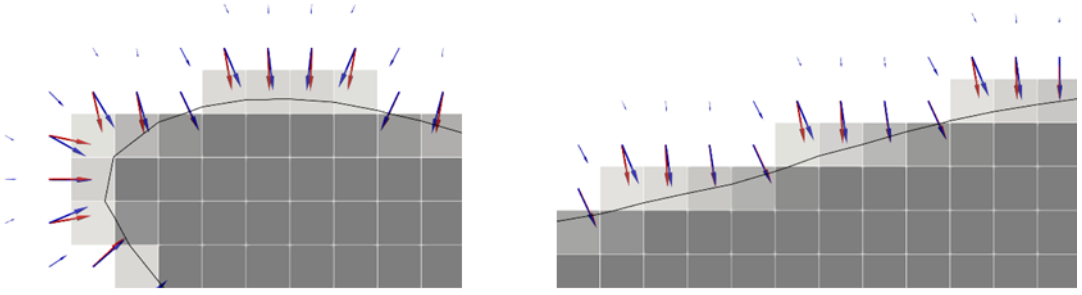

FIG. 4. Schematic illustration of normal vectors to the porous boundary: (a) example 1 with a curved porous boundary, (b) example 2 with a sloped boundary. The blue arrows represent the smoothed normal vectors given by the *hybridPorousInterFoam* solver, while the red arrows depict the smoothed normal vectors produced by the proposed method. The black lines delineate the curved or sloped porous boundary ($\varepsilon = 0.5$ iso-surface).

To model the normal to the porous boundary accurately, a weighted smoothing method is proposed in Eqs. (27) and (28). The previous and present norms to the porous boundaries are compared in FIG. 4, which shows that the present smoothed norms are successfully limited on the porous boundaries. Moreover, a visual inspection finds that the present smoothed normal vectors are more perpendicular to the curved and sloped porous boundaries than the previous smoothed normal vectors. The improved orthogonal property of the present smoothed norms can be attributed to the change in the smoothed vector from the gradient of the local porosity in Eqs. (22) and (23) to the unit normal to the porous boundary in Eqs. (27) and (28). Similar to the difference between the IG and IN schemes for computing the normal to the gas–liquid interface, as discussed in Section III.A, the adoption of the non-normalized gradient in Eqs. (22) and (23) distorts the direction of the normal to the porous boundary, which moves toward the neighboring gradient with a larger magnitude.

$$\boldsymbol{n}_{\mathrm{p}} = \frac{\nabla \varepsilon}{\left\| \nabla \varepsilon \right\|} \tag{25}$$

$$\xi = \left\| \boldsymbol{n}_{\mathrm{p}} \right\| \tag{26}$$

$$\tilde{\boldsymbol{n}}_{\mathrm{p}}^{*} = \xi \left\langle \left\langle \xi \boldsymbol{n}_{\mathrm{p}} \right\rangle_{c \to f} \right\rangle_{f \to c} \Big/ \left\langle \left\langle \xi \right\rangle_{c \to f} \right\rangle_{f \to c} \tag{27}$$

$$\tilde{\boldsymbol{n}}_{\mathrm{p},f} = \left\langle \frac{\tilde{\boldsymbol{n}}_{\mathrm{p}}^{*}}{\left\| \tilde{\boldsymbol{n}}_{\mathrm{p}}^{*} \right\|} \right\rangle_{c \to f} \tag{28}$$

D. Equation discretization

The solver is developed based on the open-source *hybridPorousInterFoam* solver,[16] which is the first implementation of the multiphase micro-continuum model with the FVM based on OpenFOAM.[51, 53, 54] The open-source code can be accessed from the author's repository (https://github.com/anoldfriend0718/multiscalePorousFoam). We welcome the interested reader to review the numerical code, reproduce simulation cases and contribute to further model development. In the FVM, the governing equations are first discretized by integrating over each control volume at the given time step to yield a set of algebraic equations. The pressure equation should be formulated by combining the semi-discretized gas continuity and DBS momentum equations to account for the velocity–pressure coupling. A detailed derivation of the semi-discretized pressure equation can be found in the literature.[16, 31] The first-order *Euler* time scheme is used to discretize the time derivative $\partial/\partial t$ terms, while the spatial terms are discretized using second-order numerical schemes. The gradient term ∇ is discretized by the *Gauss linear* scheme, with a linear scheme implemented for the value interpolation from cell centers to face centers. The *Gauss vanLeerV*

scheme is employed for the divergence term $\nabla\cdot(\frac{\rho}{\varepsilon}\bar{\boldsymbol{v}}\,\bar{\boldsymbol{v}})$, while the *Gauss vanLeer* scheme is performed for $\nabla\cdot(\alpha_{\mathrm{l}}\bar{\boldsymbol{v}})$. For the compression term in the saturation equation, the interpolation of $\alpha_{\mathrm{l}}\alpha_{\mathrm{g}}$ is implemented using the *interfaceCompression* scheme. The Laplacian term for the dissipative viscous force $\nabla\cdot\left(\mu\left(\nabla\bar{\boldsymbol{v}}+\nabla\bar{\boldsymbol{v}}^{T}\right)\right)$ is calculated using the Gauss linear corrected scheme.

E. Numerical workflow

Sequential coupling strategies are introduced to solve the discretized governing equations for the nonlinear problem, as illustrated in FIG. 5. In the numerical workflow, the pressure–velocity coupling is handled using the pressure implicit with splitting of operators (PISO) algorithm[55] to solve the DBS momentum equations. The constraint on the time step is imposed by the Brackbill condition[48] to ensure numerical stability through the explicit treatment of the surface tension force:

$$\Delta t<\sqrt{\frac{\rho_{\mathrm{ave}}\left(\Delta x\right)^{3}}{2\pi\sigma}}\,, \tag{29}$$

where ρ_{ave} is the average phase density and Δx is the grid spacing. The main iterative procedure in advancing the time step from n to n+1 is described as follows.

(1) Solve the saturation equation (6) using the multidimensional universal limiter with explicit solution (MULES) algorithm[56] to ensure the saturation boundedness;

(2) Update fluid properties such as the density ρ^{*} and viscosity μ^{*} and porous transport properties such as the relative permeability μ^{*}, phase mobility M_{i}^{*}, and capillary pressure p_{c}^{*} based on the saturation field from the previous iteration;

(3) Extrapolate the saturation $\alpha_{\mathrm{l,corr}}^{*}$ from the solid-free region to the nearby porous region according to Eq. (19) to correct the saturation gradient at the porous boundary;

(4) Calculate the normal to the gas–liquid interface $\boldsymbol{n}_{\mathrm{lg},f}^{*}$ via the hybrid formulation of Eq. (17);

(5) Compute and smooth the normal to the porous boundary $\tilde{\boldsymbol{n}}_{\mathrm{p},f}^{*}$ using Eqs. (27) and (28), and then correct the normal to the gas–liquid interface $\tilde{\boldsymbol{n}}_{\mathrm{lg},f}^{*}$ in the contact line regions according to Eq. (13);

(6) Compute the interface curvature $\bar{\kappa}^{*}$ from Eq. (14), and then update the surface tension force $\boldsymbol{F}_{\mathrm{c}}^{*}$ using Eq. (9);

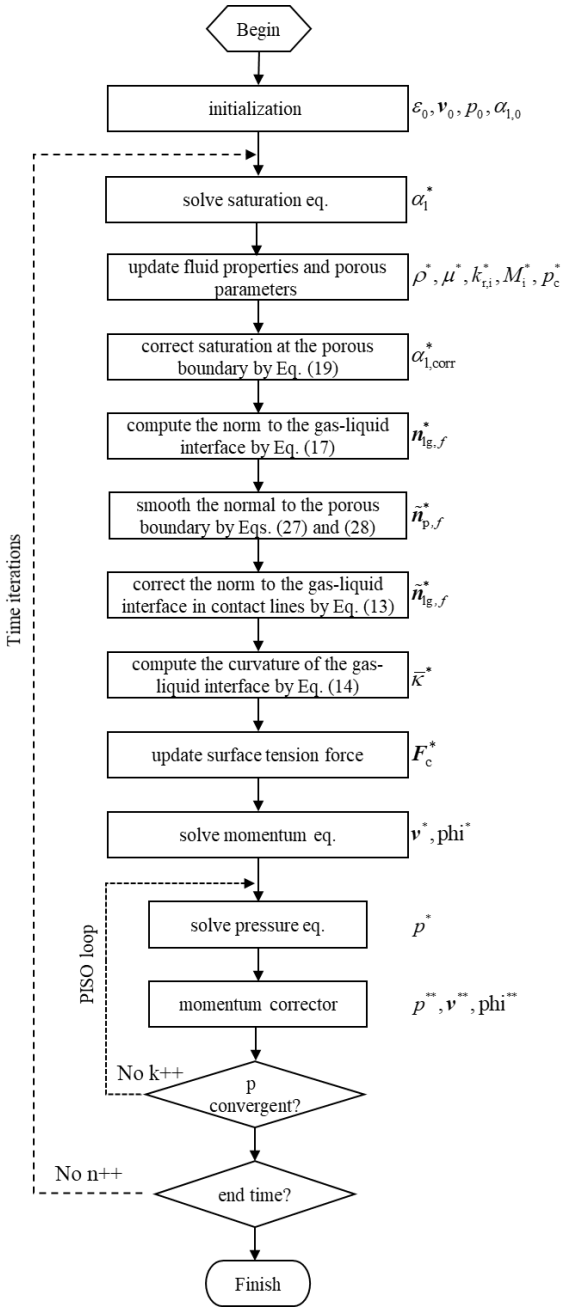

FIG. 5. Flowchart of the improved multiphase micro-continuum model.

(7) Solve the discretized DBS momentum equation (7) implicitly to predict the velocity $\bar{\boldsymbol{v}}^*$ and the mass flux phi*. Note that the predicted fields $\bar{\boldsymbol{v}}^*$ and phi* do not satisfy the mass conservation requirement after this prediction step;

(8) Solve the pressure equation implicitly with the preconditioned conjugate gradient method to correct the pressure $\bar{p}^{**}$ and update the velocity $\bar{\boldsymbol{v}}^{**}$ and mass flux phi**. This step, called the PISO loop, is repeated three times to ensure the pressure and velocity converge and satisfy the mass conservation requirement.

IV. VALIDATION CASES

A series of capillary-dominated two-phase flow tests are performed to verify that the improved micro-continuum DBS model reduces the spurious velocities. Different interpolation schemes from the interface normal to the gas–liquid interface are compared by simulating a stationary gas bubble in liquid (Section IV.A). Droplets on flat and curved surfaces with hydrophilic, neutral, and hydrophobic wettability boundary conditions are simulated to demonstrate the importance of the correction scheme of the norms to the gas–liquid interface and the weighted scheme to the porous boundary, respectively (Section IV.B). In terms of the multiphase flow dynamics in simple and complex geometries, the improved DBS model is further verified by modeling capillary rise in a single tube (Section IV.C) and liquid drainage in porous media (Section IV.D). The boundary conditions and solver parameters are defined in FIG S1-S4 and TABLE S1-S4 in the Supplementary Materials.

A. Stationary gas bubble

As a common test of two-phase flow models, simulating a gas–liquid system under equilibrium conditions enables a simple examination of the spurious velocities induced due to ill-balanced interface tension by measuring the maximum velocity in the computational domain. In this study, a stationary gas bubble in liquid is simulated without gravity to compare the spurious velocities produced by different interpolation schemes of the normal to the gas–liquid interface, including the IG, IN, and hybrid schemes. As shown in FIG. 6(a), the gas bubble of diameter $2R$ is located at the center of a square domain of length $4R$, R is 10 μm. Periodic boundary conditions are imposed on all boundaries for pressure, velocity, and liquid saturation. The fluid densities and viscosities are $\rho_l = 1000$ kg/m^3 and $\rho_g = 1$ kg/m^3, $\nu_l = 10^{-6}$ m^2/s and $\nu_g = 1.48\times10^{-5}$ m^2/s. The surface tension is $\sigma = 0.03$ kg/s^2. The impact of the mesh resolution on the spurious velocity around the stationary bubble is also investigated. TABLE II lists computational domain meshes with different resolutions of $R/\delta x$, where δx is the length of the grid cell.

TABLE II. Details of mesh and maximum time step used for the stationary gas bubble simulations.

Mesh	Mesh resolution (μm^2)	Number of cells	$R/\delta x$	Maximum time step (s)
M1	0.625×0.625	64×64	16	2.3×10^{-8}
M2	0.5×0.5	80×80	20	1.6×10^{-8}
M3	0.4×0.4	100×100	25	1.2×10^{-8}

FIG. 6 compares the liquid saturation and surface tension force fields calculated using the IG, IN, and hybrid schemes. In the magnified views of the gas–liquid interface shown in FIG. 6(b)–6(d),

the white lines represent the simulated gas–liquid interface and the black lines delineate the theoretical gas–liquid interface. Although the simulated gas–liquid interfaces are generally rounded, some deformations appear in the direction at an azimuth angle of around 45°, referred to as the 45° direction, when using the IG and IN schemes. Compared with the theoretical gas–liquid interface, the IG scheme raises the gas–liquid interface outwards, while the IN scheme collapses the gas–liquid interface inwards. The interface deformation in the 45° direction is related to the uneven surface tension forces along the circumference, as depicted in FIG. 6(e) and 6(f) for the IG and IN schemes, respectively. As discussed in Section III.A, the IG scheme underestimates the interface curvature during the numerical surface integration based on the interpolated saturation gradient. The underestimation becomes significant in the 45° direction. Consequently, the underestimated interface curvature reduces the surface tension force and eventually produces a convex gas–liquid interface. Conversely, the overpredicted interface curvature and surface tension given by the IN scheme leads to a sunken gas–liquid interface. Considering the counter-impacts of the IG and IN schemes, the hybrid scheme is intended to correct the numerical error of the interface curvature. As shown in FIG. 6(g), a relatively uniform distribution of surface tension forces can be obtained from the hybrid scheme, resulting in the closest solution to the theoretical gas–liquid interface in FIG. 6(d).

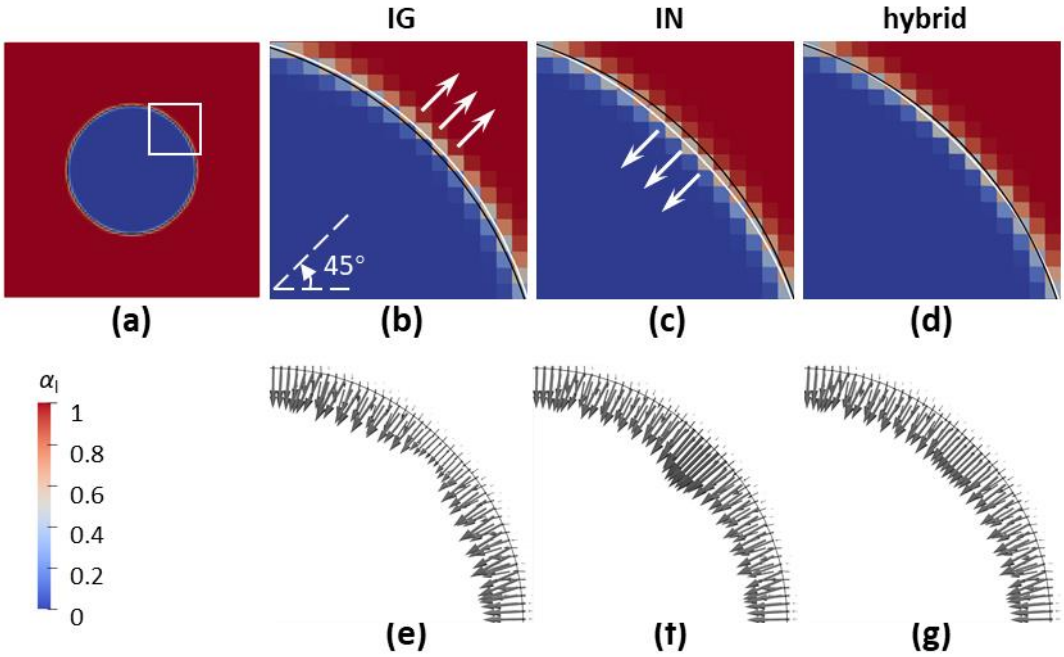

FIG. 6. Variations of simulated gas–liquid interfaces and surface tension forces under different interpolation schemes for the normal to the gas–liquid interface using the mesh resolution of $R/\delta x$=25: (a) overview of saturation field using the hybrid scheme; (b)–(d) magnified views of the gas–liquid interface using IG, IN, and hybrid schemes. The white lines represent the simulated gas–liquid interface, black lines represent the theoretical gas–liquid interface, and black arrows

represent the deformation direction; (e)–(g) magnified views of surface tension forces using IG, IN, and hybrid schemes, where gray arrows represent the surface tension force.

Besides interface deformation, the uneven surface tension force can induce spurious velocities. FIG. 7 compares the spurious capillary number using different mesh resolutions and interpolation schemes. The magnitude of the spurious velocity is defined as

$$v_{sp} = \max(|\bar{\boldsymbol{v}}|) \tag{30}$$

and the spurious capillary number is defined as

$$\mathrm{Ca}_{sp} = \frac{\mu_l v_{sp}}{\sigma}. \tag{31}$$

FIG. 7(a) indicates that the spurious capillary number computed using the IG scheme ranges from 10^{-3} to 10^{-2}, representing the largest magnitude and fluctuation among the three interpolation schemes. For the IN scheme [FIG. 7(b)], the spurious capillary number is lower than in the IG scheme, dropping to 10^{-5}–10^{-3}. In both the IG and IN schemes, the spurious capillary number increases with the mesh resolution, that is, finer grid cells. Other researchers have also reported this abnormal variation of spurious velocities with mesh resolution when using the conventional VOF model with the IG or IN scheme.[44, 57] One possible reason is that the curvature computation with a finer mesh is more sensitive to numerical errors in the normal vector to the gas–liquid interface than a coarse mesh. By comparison, FIG. 7(c) shows that the spurious capillary number using the hybrid scheme converges to about 10^{-5}, regardless of the mesh resolution, even though the finer mesh yields more rapid convergence. This implies that the hybrid scheme is the most robust solution for achieving low spurious velocities with various mesh sizes.

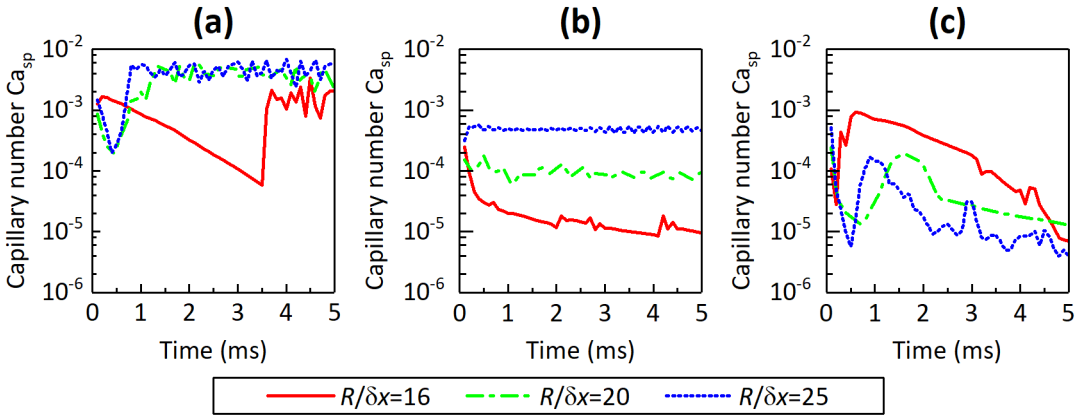

FIG. 7. Spurious capillary number based on the spurious velocities versus time using different mesh resolutions and interpolation schemes: (a) IG, (b) IN, (c) hybrid.

These results show that the IG and IN schemes cause interface deformations in opposite direction due to the underestimated and overestimated surface tension forces. The proposed hybrid scheme produces more accurate curvature values, effectively mitigating the interface deformation and robustly reducing the spurious velocity to spurious capillary numbers of less than 10^{-5} under

various mesh resolutions. What should be emphasized is that the hybrid scheme for the normal to the gas–liquid interface is implemented based on the CSF model rather than the SSF model or its variations. Even though the SSF model can reduce the spurious capillary number of static gas bubbles to the level of machine precision (10^{-15}),[9] spurious currents still emerge when simulating the multiphase flow dynamics in capillary-dominated regimes with $Ca \leq 10^{-4}$. Section IV.D will show that spurious currents of acceptable magnitude can also be achieved by the hybrid scheme based on the CSF model with $Ca=10^{-4}$. In addition, considerable modifications must be applied to the interface dynamics in the SSF model,[52] including smoothed saturation by a Laplacian smoother for the calculation of interface curvature and sharpened saturation by a curtailment function for the computation of the surface tension force.[9] For these reasons, the combination of the hybrid scheme and the CSF model is used in the present study to ensure the numerical model is simple, physical, and effective.

B. Stationary droplets on flat and curved surfaces

Using a classic test of stationary droplets on flat surfaces, the effect of the norm correction to the gas–liquid interface at the porous boundary on the contact-line dynamics is investigated to verify the improved DBS model. Particular attention is given to the contact angle and the spurious velocity in the contact-line region at the equilibrium state. A semicircle droplet with a radius of 0.7 mm is initialized on a flat surface, and three different contact angles of $\theta = 60°, 90°, 135°$ are prescribed. In the micro-continuum DBS model, a porous plate with negligible porosity and permeability ($\varepsilon = 0.01$, $k_0 = 10^{-16}\,\mathrm{m}^{-2}$) is introduced to approximate the nonslip wall boundary based on a penalization strategy.[15] To highlight the necessity of the saturation extrapolation algorithm during the norm correction, a contrasting saturation is set up on the sides of the porous boundary, where the porous substrate is saturated with the liquid, while the gas fills the upper clear fluid region except for the liquid droplet. The fluid densities and viscosities in each phase are set as $\rho_l = 1000$ kg/m^3 and $\rho_g = 1$ kg/m^3, $\nu_l = 10^{-6}\,\mathrm{m}^2/\mathrm{s}$ and $\nu_g = 1.48\times10^{-5}$ m^2/s, respectively. The surface tension is $\sigma = 0.03$ kg/s^2. The computation is configured with a cell size of 12.5 μm and a time step of 0.5 μs.

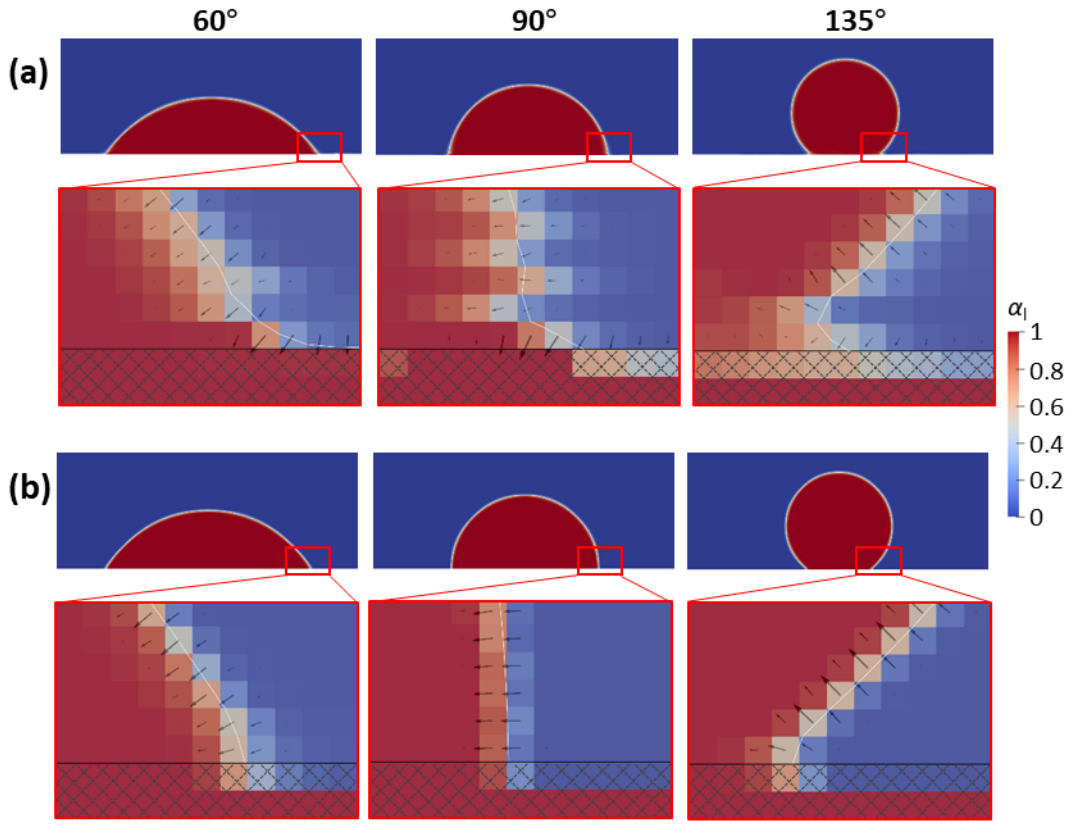

FIG. 8. Liquid saturation fields of droplets on flat surfaces with different prescribed contact angles using: (a) original DBS and (b) improved DBS with saturation gradient correction. The solid white lines represent the gas–liquid interface ($\alpha_l = 0.5$ iso-surface), the solid black lines represent the fluid–solid interface ($\varepsilon = 0.5$ iso-surface), black arrows represent the saturation gradient, and gray diagonals represent the porous region.

FIG. 8 compares the equilibrium saturation configurations of these droplets on flat surfaces with three contact angles, each computed using the micro-continuum DBS model with and without correcting the normal to the gas–liquid interface. In the magnified views of the contact-line region, the simulated gas–liquid interface is delineated by the white line, and the saturation gradient is represented by black arrows to visualize the cause of the numerical error in the contact angle. As observed in FIG. 8(a) for the original DBS results, the contrasting saturation introduces nonzero saturation gradients at the porous boundary, which should be zero in the conventional VOF approach using the standard wall boundary rather than the porous plate. The resulting normal vector to the gas–liquid interface $\boldsymbol{n}_{\mathrm{lg}}$ deviates from its original definition in the contact angle correction algorithm of Eq. (13). The numerical error then propagates from the normal vector to the gas–liquid interface $\boldsymbol{n}_{\mathrm{lg}}$ into the capillary force $\boldsymbol{F}_{\mathrm{c}}$ based on Eq. (9). Consequently, FIG. 9(a) clearly illustrates that significant spurious velocities emerge at the contact-line region. FIG. 10(a) quantifies

the spurious velocity as ranging from 0.002–0.025 m/s. Furthermore, it is interesting that, compared with the hydrophilic contact angle of $\theta = 45°$, the spurious velocity is mitigated with the hydrophobic contact angle of $\theta = 135°$. This is because, when the hydrophobic system reaches equilibrium, the decreasing saturation in the first layer of the porous plate reduces the saturation gradient and weakens the non-physical capillary force. The saturation extrapolation algorithm enforces zero saturation gradients at the porous boundary based on Eqs. (18)–(19) so that the normal to the gas–liquid interface $\boldsymbol{n}_{lg}$ is consistent with that of the conventional VOF approach. FIG. 8(b) shows that the improved DBS model yields a contact angle that is almost identical to the prescribed value, regardless of whether the configuration is hydrophobic or hydrophilic. Correspondingly, FIG. 9(b) shows that the spurious velocity of the improved DBS model is virtually zero if the contour color bar is set with the same scale as the original DBS model. In quantitative comparison with the original DBS model, FIG. 10(a) shows that the improved DBS model reduces the spurious velocity by about one order of magnitude to less than 10^{-3} m/s, which is close to the spurious velocity around the gas–liquid interface far away from the contact line.

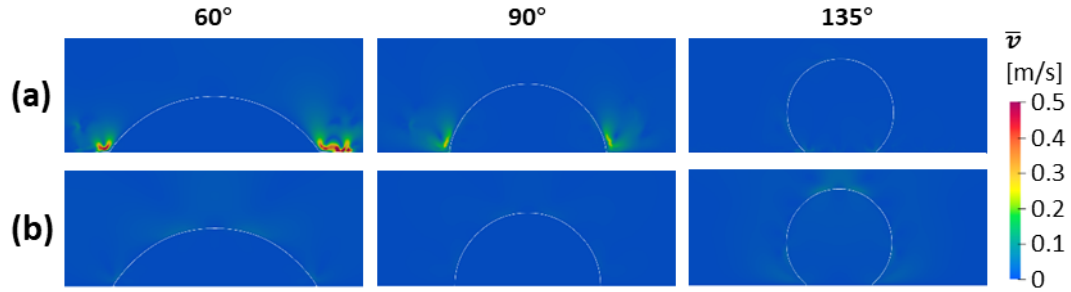

FIG. 9. Velocity fields of droplets on flat surfaces with different prescribed contact angles using: (a) original DBS and (b) improved DBS with saturation gradient correction. Solid white lines represent the gas–liquid interface ($\alpha_l = 0.5$ iso-surface).

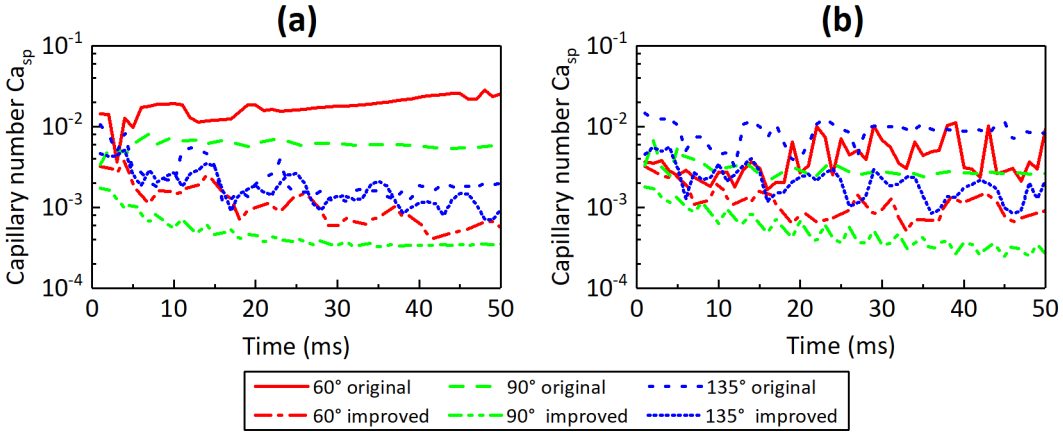

FIG. 10. Spurious capillary number versus time: (a) droplets on flat surfaces simulated by the

original DBS and the improved DBS with saturation gradient correction, (b) droplets on curved surfaces simulated by the original DBS and the improved DBS with saturation gradient correction and smoothed norms.

570 Furthermore, a droplet on a curved surface is simulated to illustrate the influence of the
571 weighted smoothing scheme of the normal to the porous boundary on the contact-line dynamics
572 along a complex boundary. As discussed in Section III.C, the weighted smoothing scheme improves
573 the orthogonality of the normal to the porous boundary, which is approximated with a staircase mesh
574 in the micro-continuum model. Additionally, the weighted smoothing scheme constricts the nonzero
575 norm in the sharp vicinity of the porous boundary. By comparing the spurious velocity contours
576 obtained from the original and improved DBS models, FIG. 11 demonstrates that the spurious
577 velocity is significantly reduced by the weighted smoothing scheme, implying an improved force
578 balance at the curved contact line. Quantitatively, FIG. 10(b) shows that the spurious velocities are
579 reduced by one order of magnitude for contact angles of 60° and 90°, and by 70% for a contact
580 angle of 135°.

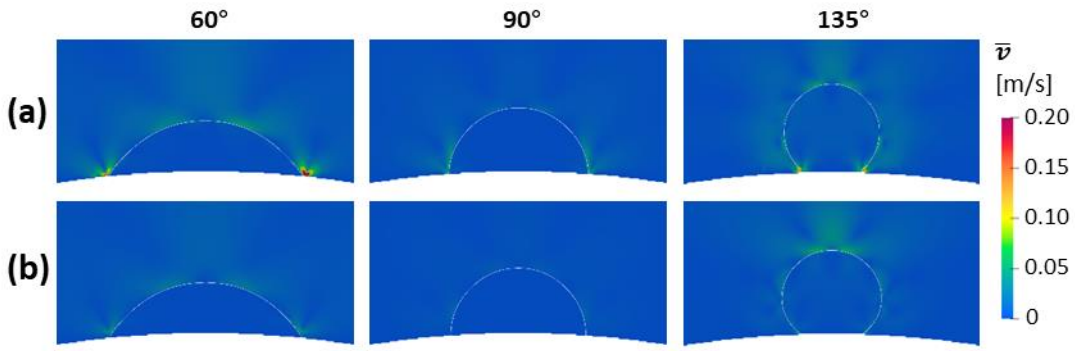

FIG. 11. Velocity fields of droplets on curved surfaces with different prescribed contact angles using: (a) original DBS and (b) improved DBS with the saturation gradient correction and the smoothed normal to the porous boundary. Solid white lines represent the gas–liquid interface ($\alpha_l = 0.5$ iso-surface).

581 These results show that the improved DBS model achieves a more accurate contact angle than
582 the original DBS model and reduces the spurious velocity by about one order of magnitude. These
583 improvements are achieved by combining the correction scheme for the normal to the gas–liquid
584 interface with the weighted smoothing scheme for the normal to the porous boundary.
585
586 **C. Capillary rise**
587 In terms of multiphase flow, this section simulates the capillary rise of a liquid through a narrow
588 tube using the original and improved micro-continuum DBS models, and compares the accuracy
589 against the conventional VOF model. The conventional VOF model is solved by the *interFoam*
590 solver. As shown in FIG. 12(a), the fluid domain extends over 1 mm × 20 mm and is discretized

with a uniform mesh of 20 × 400. On the left and right boundaries, the conventional VOF model adopts the standard no-slip wall condition, while the micro-continuum model uses impermeable porous plates for approximations, as in Section IV.B. The fluid densities and viscosities are $\rho_l = 1000$ kg/m^3 and $\rho_g = 1$ kg/m^3, $\nu_l = 10^{-6}$ m^2/s and $\nu_g = 1.48\times10^{-5}$ m^2/s. The surface tension is $\sigma = 0.07$ kg/s^2, and the contact angle on the wall or porous boundary is prescribed as 45°. The initial meniscus is set up about 2 mm lower than the analytical equilibrium height. The rising height reaches equilibrium when the vertical component of the surface tension force is balanced by the gravitational force of the risen liquid column, which can be analytically calculated as

$$h_{eq} = \frac{2\sigma\cos\theta}{\Delta\rho|\boldsymbol{g}|d}, \tag{32}$$

where d is the tube diameter and $\Delta\rho = \rho_l - \rho_g$ is the density difference between the gas and liquid phases. The simulated equilibrium height is estimated as

$$h'_{eq} = \frac{\int_S \alpha_l dS}{d}. \tag{33}$$

FIG. 12(a)–12(c) present the steady-state liquid saturation fields computed by the original DBS, improved DBS, and conventional VOF models. FIG. 13(a) compares their equilibrium heights with the analytical result. As can be observed, the equilibrium height predicted by the improved DBS model shows the best agreement with the analytical result, with a relative error of -1.9%. The original DBS and the conventional VOF models are comparable, both significantly underestimating the equilibrium height with a relative error of -8.9%. Similar to the present results, some previous studies have found that the conventional VOF model with the *interFoam* solver overpredicts the contact angle and underestimates the equilibrium height.[16]

Furthermore, FIG. 12(d)–12(f) delineate the gas–liquid interfaces and highlight the spurious velocities near the interface. The gas–liquid interface predicted by the original DBS model exhibits noticeable deformation near the contact-line region. Even worse, considerable spurious velocities appear near both the gas–liquid interface and contact-line region. However, the improved DBS model largely eliminates the spurious currents, to even lower levels than the conventional VOF model, due to the well-balanced surface tension force and the improved contact-line dynamics. For a more intuitive analysis, FIG. 13(b) compares the spurious capillary numbers of the three multiphase models. By comparison, the improved DBS model reduces the spurious velocity by at least one order of magnitude compared with the conventional VOF model and by about two orders of magnitude compared with the original DBS model. This benchmark demonstrates that the improved DBS model can achieve minimal spurious capillary numbers of around 10^{-4} when multiphase flow dynamics are accounted for.

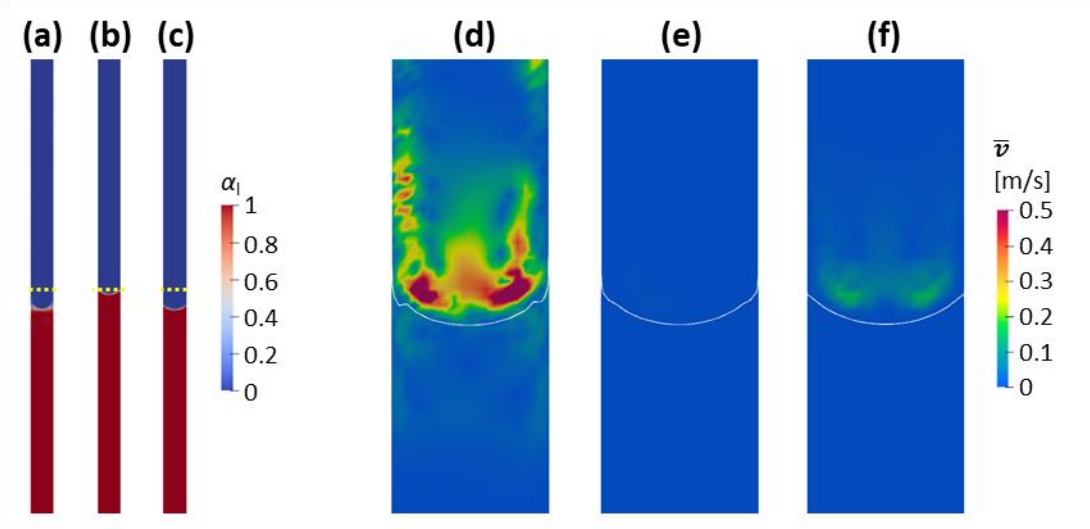

FIG. 12. Liquid saturation fields (t=2 s) for the capillary rise cases: (a) original DBS, (b) improved DBS, (c) conventional VOF; and velocity fields near the gas–liquid interface: (d) original DBS, (e) improved DBS, (f) conventional VOF. The gas–liquid interfaces are represented by white solid lines, and the analytical equilibrium height (9.91 mm) is represented by the yellow dotted lines.

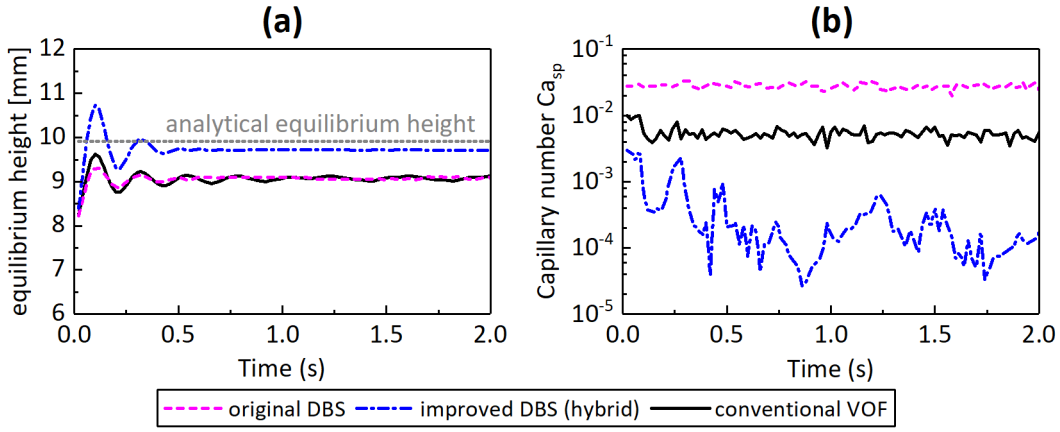

FIG. 13. Comparison of different models over time: (a) simulated equilibrium height, (b) spurious capillary number.

D. Liquid drainage in a porous medium

In this section, pore-scale simulations of liquid drainage are performed to illustrate the applicability of the improved DBS model to capillary-dominated two-phase flow in complex porous media. This case is mainly concerned about pore-scale simulations of flow and transport in porous media, thus the effect of reservoir edge cannot directly affect the physics in such small-sized region. The computational domain is 960 μm × 230 μm in size and is meshed with a 960 × 230 Cartesian grid, and the pore size is about 50 μm. For the micro-continuum model, the porosity is set to one in clean fluid regions and close to zero in the solid grains. This allows the solid grains to yield an

absolute permeability of 10^{-16} m^{-2} and reproduces the nonslip velocity condition on the surface by penalization. To create the equivalent computational domain for the conventional VOF model, solid-grain-occupied cells are removed from the mesh and replaced by rectangular and triangular cells to match the grain geometry via the OpenFOAM *snappyHexMesh* utility. The body-fitted grain surface is then assigned as a nonslip boundary and shares the same wettability condition as the micro-continuum model. The computational domain is initially saturated with gas, denoted as "g," and non-wetting liquid ($\theta = 135°$), denoted as "l," is injected from the left inlet at a velocity of $v_0 = 0.005$ m/s. The fluid densities and viscosities are $\rho_l = 1000$ kg/m^3 and $\rho_g = 20$ kg/m^3, $\nu_l = 10^{-6}$ m^2/s and $\nu_g = 1.48\times10^{-5}$ m^2/s. Surface tension values of $\sigma = 0.005$ kg/s^2, 0.01 kg/s^2, and 0.05 kg/s^2 are used to produce inlet capillary numbers $Ca = \mu_l v_0 / \sigma$ ranging from 10^{-3} to 10^{-4}, allowing us to examine various spurious velocities and their impact on the multiphase flow dynamics.

FIG. 14 presents the displacement pattern and saturation distribution at the end of the simulation when the invading fluid reaches the other side of the computational domain, as solved by the original DBS, improved DBS, and conventional VOF models. The gas–liquid displacement produces a typical capillary fingering pattern. The injected liquid prefers to invade the larger pores due to the lower entry capillary resistance. The fingering grows in both the longitudinal and lateral directions, despite the longitudinal fingering proceeding slightly faster in this case. When Ca is greater than 10^{-4}, the three simulation results are similar, creating the same preferential pathways and the same breakthrough at 50 ms. Some minor differences in the saturation distribution between the micro-continuum and the conventional VOF models can be observed. This can be attributed to the different mesh structures representing the solid grain geometry. Nevertheless, when Ca=10^{-4}, the leading fingering edge predicted by the original DBS model lags behind that simulated by the improved DBS model and the conventional VOF model. The varying multiphase flow dynamics are related to the presence of spurious currents, as shown in FIG. 15. The spurious currents can be observed in the original DBS simulation result at Ca=5×10^{-4}, and become significantly intensified at Ca=10^{-4}. From the magnified views of the local saturation and velocity fields for Ca=10^{-4} in FIG. 16, the spurious velocities presented in the original DBS results are much more remarkable than the physical velocity, particularly at the corner-line regions. Quantitative comparisons in FIG. 17 indicate that the improved DBS model substantially reduces the spurious velocity by one order of magnitude to a level comparable to the conventional VOF model. These observations suggest that the improved DBS model can accurately simulate the multiphase flow dynamics in the capillary-dominated regime at Ca ~ 10^{-4} due to the limited spurious velocity, even in complicated porous media. Regarding the comparable simulations to the conventional VOF model, the improved

contact-line dynamics given by the correction scheme of the normal to the gas–liquid interface and the weighted smoothing scheme of the normal to the porous boundary play an essential role in limiting the spurious velocities.

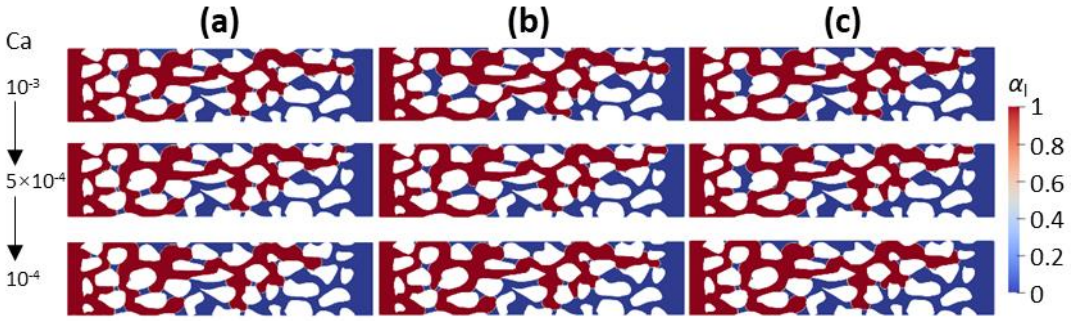

FIG. 14. Displacement patterns at breakthrough (t=50 ms) for different capillary numbers using: (a) original DBS model, (b) improved DBS model, and (c) conventional VOF model.

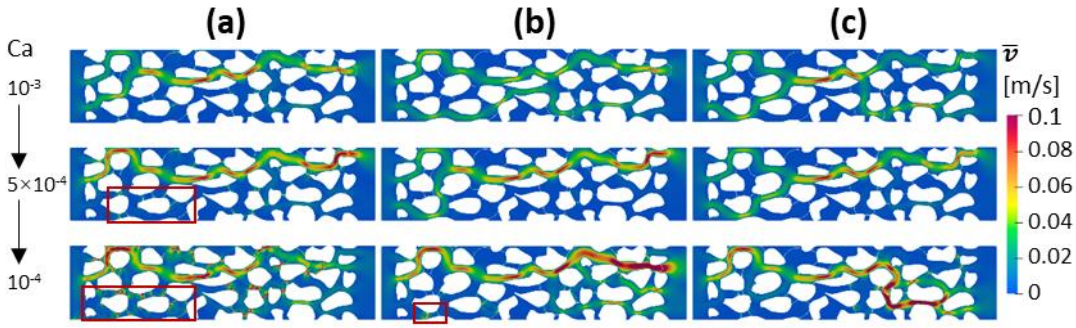

FIG. 15. Velocity fields (t=50 ms) for different capillary numbers using: (a) original DBS model, (b) improved DBS model, and (c) conventional VOF model.

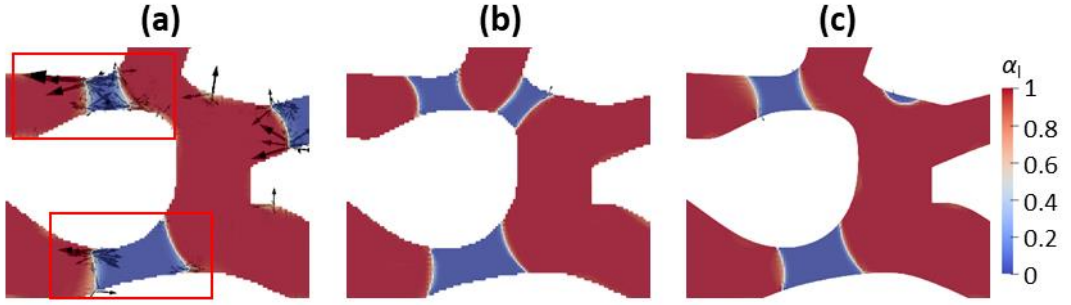

FIG. 16. Magnified views of local saturation and velocity fields (t=50 ms) for an inlet capillary number of Ca=10^{-4} using: (a) original DBS model, (b) improved DBS model, and (c) conventional VOF model. White lines represent the gas–liquid interface and black arrows quantify the magnitude and direction of velocity vectors.

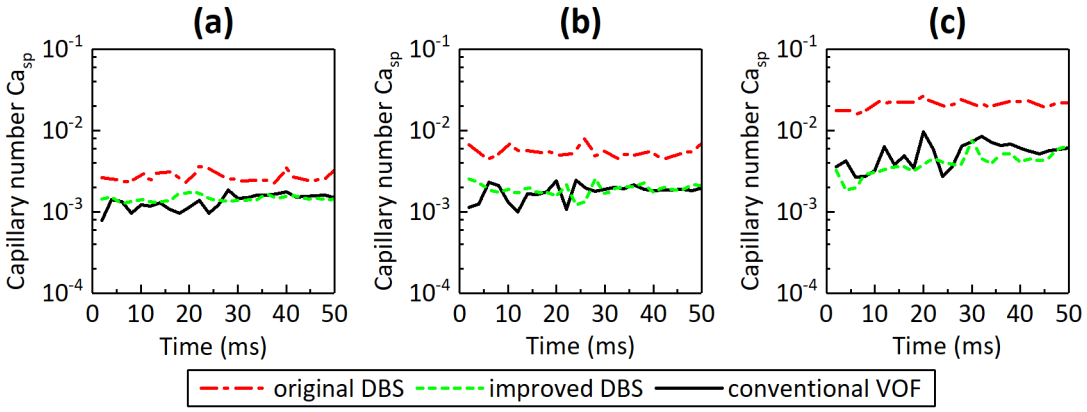

FIG. 17. Time-dependent spurious capillary number based on the maximum velocity calculated by the original DBS model, improved DBS model, and conventional VOF model: (a) $Ca=10^{-3}$, (b) $Ca=5\times10^{-4}$, (c) $Ca=10^{-4}$.

These four illustrative cases show the ability of the improved DBS model to simulate capillary-dominated multiphase flows at the pore scale. During verification, some benchmark results were provided by the conventional VOF model, implying that the micro-continuum model can successfully recover known multiphase Navier–Stokes solutions when used as a pore-scale model. Not limited to the pore scale, previous studies[14, 16] have clearly demonstrated that the micro-continuum model has the ability to simulate multiphase Darcy flows when used as a continuum-scale model and multiscale multiphase dynamics when used as a hybrid-scale model. The contribution of the present study is the development of an improved DBS model in mitigating spurious velocities, leading to an enhanced capacity in the capillary-dominated regime. In further work, multiphase reactive transport flows with heterogeneous reactions in porous media, such as hydrate dissociation, will be investigated to demonstrate that the improved DBS model has the capacity to solve complex multiscale problems, typically with capillary numbers of around 10^{-4}.

V. CONCLUSIONS

The present study has improved the multiphase micro-continuum DBS model to enable accurate simulations of two-phase flows at capillary numbers as low as 10^{-4}. A hybrid interpolation scheme was proposed to improve the accuracy of the normal to the gas–liquid interface and the interface curvature. At the porous boundary, the normal to the gas–liquid interface was revised by a saturation extrapolation scheme to exclude the impact of saturation in the unresolved porous regions on the contact angle correction. To further guarantee the accurate contact angle correction at the curved surface, a weighted smoothing scheme was constructed to enhance the orthogonal property of the normal to the porous boundary and constrain the nonzero norm at the porous boundary. Compared with the original DBS model,[16] the combination of these three schemes theoretically improves the force balance and mitigates the spurious velocities at the gas–liquid interface and

contact lines.

Four benchmark cases were investigated to verify the numerical performance of the improved DBS model. First, the impact of different interpolation schemes for the normal to the gas–liquid interface on the interfacial dynamics was investigated by simulating a static gas bubble in liquid. The IG interpolation scheme used in the *interFoam*[51] and *hybridPorousInterFoam*[16] solvers was found to underestimate the interface curvature and surface tension force, leading to a convex gas–liquid interface. Conversely, the IN interpolation scheme used in the *poreFoam*[9, 44] and *interGCFoam*[52] solvers overpredicted the interface curvature and surface tension force, resulting in a sunken gas–liquid interface. The hybrid interpolation scheme eliminated the interface deformation and robustly reduced the spurious velocity at the gas–liquid interface by one or two orders of magnitude compared with the IG or IN scheme. Second, stationary droplets on flat and curved surfaces were simulated. The results prove that the improved DBS model has the ability to target the prescribed contact angle and decrease the spurious velocity at the contact-line region by about one order of magnitude compared with the original DBS model. In the third and fourth examples, capillary rise and liquid drainage in a porous medium were simulated to demonstrate that the improved DBS model can simulate capillary-dominated multiphase flows with negligible spurious velocities at $Ca=10^{-4}$ in simple and complex geometries, respectively.

The improved model effectively reduces the spurious velocity for capillary-dominated multiphase flow to the order of the traditional VOF method using the body-fitted meshes. However, the computational efficiency of the DBS model is still not good enough. For example, the fourth test case, which involves multiphase flow in a porous medium meshing 69600 grid blocks, requires 64 CPU cores to complete the computation in about 20 minutes for a physical time of 0.05 seconds.

In future work, the improved DBS model needs more physics incorporations to simulate the multiphase reactive flows within multiscale structures. And the computational efficiency will be improved by removing unused solid phases from the computational domain and optimizing the solver algorithms. After verifying the improved DBS method with other multiscale solvers and experimental results, hybrid-scale simulations will be performed on specific scenarios including carbonate dissolution and methane hydrate dissociation, to understand the effect of sub-resolution porosity on multiphase reactive flow in the natural multiscale rock.

SUPPLEMENTARY MATERIAL

The boundary conditions and simulation parameters of the validation cases can be found in the Supplementary Material.

ACKNOWLEDGMENTS

This work is supported by the National Natural Science Foundation of China (No. 51876100

& 52206014 & 52176011), and the Open-Project Program of the State Key Laboratory of Chemical Engineering (No. SKL-ChE-21A04).

DECLARATION OF INTERESTS

The authors declare that they have no known competing financial interests or personal relationships that could have appeared to influence the work reported in this paper.

DATA AVAILABILITY STATEMENT

The data that support the findings of this study are available from the corresponding author upon reasonable request.

AUTHOR CONTRIBUTIONS

Zhiying Liu: Conceptualization (lead); Methodology (lead); Validation (equal); Writing – original draft (lead).

Junyu Yang: Conceptualization (supporting); Methodology (supporting); Validation (equal).

Qianghui Xu: Writing – original draft (supporting); Writing – review and editing (equal); Supervision (equal); Funding Acquisition (equal).

Lin Shi: Writing – review and editing (equal); Supervision (equal); Funding Acquisition (equal).

REFERENCES

[1]S. Bakhshian, "Dynamics of dissolution trapping in geological carbon storage," Int. J. Greenhouse Gas Control **112**, 103520 (2021).

[2]A. S. Ambekar, S. Mondal, andV. V. Buwa, "Pore-resolved volume-of-fluid simulations of two-phase flow in porous media: Pore-scale flow mechanisms and regime map," Phys. Fluids **33**, 102119 (2021).

[3]J. Yang, X. Dai, Q. Xu, Z. Liu, C. Zan, W. Long, andL. Shi, "Pore-scale study of multicomponent multiphase heat and mass transfer mechanism during methane hydrate dissociation process," Chem. Eng. J. **423**, 130206 (2021).

[4]M. Karimzadeh, M. Khatibi, S. N. Ashrafizadeh, andP. K. Mondal, "Blue energy

generation by the temperature-dependent properties in funnel-shaped soft nanochannels," Phys. Chem. Chem. Phys. **24**, 20303 (2022).

[5]A. Ganjizade, S. N. Ashrafizadeh, andA. Sadeghi, "Effect of ion partitioning on the electrostatics of soft particles with a volumetrically charged core," Electrochem. Commun. **84**, 19 (2017).

[6]M. Karimzadeh, Z. Seifollahi, M. Khatibi, andS. N. Ashrafizadeh, "Impacts of the shape of soft nanochannels on their ion selectivity and current rectification," Electrochim. Acta **399**, (2021).

[7]M. Stefanoni, U. M. Angst, andB. Elsener, "Kinetics of electrochemical dissolution of metals in porous media," Nat. Mater. **18**, 942 (2019).

[8]S. S. Datta, J.-B. Dupin, andD. A. Weitz, "Fluid breakup during simultaneous two-phase flow through a three-dimensional porous medium," Phys. Fluids **26**, 062004 (2014).

[9]A. Q. Raeini, M. J. Blunt, andB. Bijeljic, "Modelling two-phase flow in porous media at the pore scale using the volume-of-fluid method," J. Comput. Phys. **231**, 5653 (2012).

[10]M. Miarelli, andA. Della Torre, "Workflow Development to Scale up Petrophysical Properties from Digital Rock Physics Scale to Laboratory Scale," Transp. Porous Media **140**, 459 (2021).

[11]L. C. Ruspini, P. E. Øren, S. Berg, S. Masalmeh, T. Bultreys, C. Taberner, T. Sorop, F. Marcelis, M. Appel, J. Freeman, andO. B. Wilson, "Multiscale Digital Rock Analysis for Complex Rocks," Transp. Porous Media **139**, 301 (2021).

[12]B. Guo, L. Ma, andH. A. Tchelepi, "Image-based micro-continuum model for gas flow in organic-rich shale rock," Adv. Water Resour. **122**, 70 (2018).

[13]K. Miller, T. Vanorio, S. Yang, andX. Xiao, "A scale-consistent method for imaging porosity and micrite in dual-porosity carbonate rocks," Geophysics **84**, MR115 (2019).

[14]C. Soulaine, P. Creux, andH. A. Tchelepi, "Micro-continuum framework for pore-scale multiphase fluid transport in shale formations," Transp. Porous Media **127**, 85 (2019).

[15]C. Soulaine, andH. A. Tchelepi, "Micro-continuum approach for pore-scale simulation of subsurface processes," Transp. Porous Media **113**, 431 (2016).

[16]F. J. Carrillo, I. C. Bourg, andC. Soulaine, "Multiphase flow modeling in multiscale porous media: An open-source micro-continuum approach," J. Comput. Phys.: X **8**, 100073 (2020).

[17]S. Whitaker, "Flow in porous media I: A theoretical derivation of Darcy's law," Transp. Porous Media **1**, 3 (1986).

[18]C. Soulaine, S. Roman, A. Kovscek, andH. A. Tchelepi, "Pore-scale modelling of multiphase reactive flow: application to mineral dissolution with production CO_2," J. Fluid Mech. **855**, 616 (2018).

[19]M. T. Van Genuchten, "A closed‐form equation for predicting the hydraulic conductivity of unsaturated soils," Soil Sci. Soc. Am. J. **44**, 892 (1980).

[20]R. H. Brooks, *Hydraulic properties of porous media* (Colorado State University, 1965).

[21]M. Starnoni, andD. Pokrajac, "On the concept of macroscopic capillary pressure in two-phase porous media flow," Adv. Water Resour. **135**, 103487 (2020).

[22]G. Neale, andW. Nader, "Practical significance of brinkman's extension of darcy's law: Coupled parallel flows within a channel and a bounding porous medium," Can. J. Chem. Eng. **52**, 475 (1974).

[23]F. Golfier, B. Bazin, R. Lenormand, andM. Quintard, "Core-scale description of porous media dissolution during acid injection - Part I: theoretical development," Comput. Appl. Math. **23**, 173 (2004).

[24]F. Golfier, C. Zarcone, B. Bazin, R. Lenormand, D. Lasseux, andM. Quintard, "On the ability of a Darcy-scale model to capture wormhole formation during the dissolution of a porous medium," J. Fluid Mech. **457**, 213 (2002).

[25]H. Luo, F. Laouafa, G. Debenest, andM. Quintard, "Large scale cavity dissolution: From the physical problem to its numerical solution," Eur. J. Mech. B. Fluids **52**, 131 (2015).

[26]H. Luo, F. Laouafa, J. Guo, andM. Quintard, "Numerical modeling of three-phase dissolution of underground cavities using a diffuse interface model," Int. J. Numer. Anal. Methods Geomech. **38**, 1600 (2014).

[27]H. Luo, M. Quintard, G. Debenest, andF. Laouafa, "Properties of a diffuse interface model based on a porous medium theory for solid–liquid dissolution problems," Comput. Geosci. **16**, 913 (2012).

[28]G. S. Beavers, andD. D. Joseph, "Boundary conditions at a naturally permeable wall,"

J. Fluid Mech. **30**, 197 (1967).

[29]T. C, Hsu; P, Cheng, "Thermal dispersion in a porous medium," Int. J. Heat Mass Transfer **33**, 1587 (1990).

[30]H. C. Brinkman, "A calculation of the viscous force exerted by a flowing fluid on a dense swarm of particles," Flow, Turbul. Combust. **1**, 27 (1949).

[31]Q. Xu, X. Dai, J. Yang, Z. Liu, andL. Shi, "Image-based modelling of coke combustion in a multiscale porous medium using a micro-continuum framework," J. Fluid Mech. **932**, A51 (2022).

[32]S. Whitaker, *The method of volume averaging* (Springer Science & Business Media, 2013).

[33]T. D. Scheibe, W. A. Perkins, M. C. Richmond, M. I. McKinley, P. D. J. Romero-Gomez, M. Oostrom, T. W. Wietsma, J. A. Serkowski, andJ. M. Zachara, "Pore-scale and multiscale numerical simulation of flow and transport in a laboratory-scale column," Water Resour. Res. **51**, 1023 (2015).

[34]C. Soulaine, S. Roman, A. Kovscek, andH. A. Tchelepi, "Mineral dissolution and wormholing from a pore-scale perspective," J. Fluid Mech. **827**, 457 (2017).

[35]F. Yang, A. G. Stack, andV. Starchenko, "Micro-continuum approach for mineral precipitation," Sci. Rep. **11**, 1 (2021).

[36]C. S. Julien Maes, Hannah P. Menke, "Improved Volume-of-Solid formulations for micro-continuum simulation of mineral dissolution at the pore-scale," arXiv:2204.07019 [physics.flu-dyn] (2022).

[37]H. Dartoomi, M. Khatibi, andS. N. Ashrafizadeh, "Importance of nanochannels shape on blue energy generation in soft nanochannels," Electrochim. Acta **431**, (2022).

[38]H. Dartoomi, M. Khatibi, andS. N. Ashrafizadeh, "Nanofluidic Membranes to Address the Challenges of Salinity Gradient Energy Harvesting: Roles of Nanochannel Geometry and Bipolar Soft Layer," Langmuir **38**, 10313 (2022).

[39]F. J. Carrillo, C. Soulaine, andI. C. Bourg, "The impact of sub-resolution porosity on numerical simulations of multiphase flow," Adv. Water Resour. **161**, (2022).

[40]Q. Zhang, H. Deng, Y. Dong, S. Molins, X. Li, andC. Steefel, "Investigation of Coupled Processes in Fractures and the Bordering Matrix via a Micro‐Continuum Reactive Transport Model," Water Resour. Res. **58**, (2022).

[41]X. He, M. AlSinan, Z. Zhang, H. Kwak, andH. Hoteit, *Micro-Continuum Approach for Modeling Coupled Flow and Geomechanical Processes in Fractured Rocks* (2022).

[42]H. Deng, J. Poonoosamy, andS. Molins, "A reactive transport modeling perspective on the dynamics of interface-coupled dissolution-precipitation," Appl. Geochem. **137**, (2022).

[43]P. Horgue, M. Prat, andM. Quintard, "A penalization technique applied to the “Volume-Of-Fluid” method: Wettability condition on immersed boundaries," Comput. Fluids **100**, 255 (2014).

[44]M. Shams, A. Q. Raeini, M. J. Blunt, andB. Bijeljic, "A numerical model of two-phase flow at the micro-scale using the volume-of-fluid method," J. Comput. Phys. **357**, 159 (2018).

[45]R. Scardovelli, andS. Zaleski, "Direct numerical simulation of free-surface and interfacial flow," Annu. Rev. Fluid Mech. **31**, 567 (1999).

[46]B. Zhao, C. W. Macminn, B. K. Primkulov, Y. Chen, A. J. Valocchi, J. Zhao, Q. Kang, K. Bruning, J. E. McClure, C. T. Miller, A. Fakhari, D. Bolster, T. Hiller, M. Brinkmann, L. Cueto-Felgueroso, D. A. Cogswell, R. Verma, M. Prodanović, J. Maes, S. Geiger, M. Vassvik, A. Hansen, E. Segre, R. Holtzman, Z. Yang, C. Yuan, B. Chareyre, andR. Juanes, "Comprehensive comparison of pore-scale models for multiphase flow in porous media," Proc. Natl. Acad. Sci. U. S. A. **116**, 13799 (2019).

[47]S. Fagbemi, P. Tahmasebi, andM. Piri, "Pore-scale modeling of multiphase flow through porous media under triaxial stress," Adv. Water Resour. **122**, 206 (2018).

[48]J. U. Brackbill, D. B. Kothe, andC. Zemach, "A continuum method for modeling surface tension," J. Comput. Phys. **100**, 335 (1992).

[49]C. K. Tam, "The drag on a cloud of spherical particles in low Reynolds number flow," J. Fluid Mech. **38**, 537 (1969).

[50]P. Meakin, andA. M. Tartakovsky, "Modeling and simulation of pore-scale multiphase fluid flow and reactive transport in fractured and porous media," Rev. Geophys. **47**, (2009).

[51]H. Jasak, A. Jemcov, andZ. Tukovic, *OpenFOAM: A C++ library for complex physics simulations* (IUC Dubrovnik Croatia, 2007).

[52]J. Maes, andH. P. Menke, "GeoChemFoam: Direct Modelling of Multiphase Reactive Transport in Real Pore Geometries with Equilibrium Reactions," Transp. Porous Media

882 **139**, 271 (2021).

883 [53]H. Jasak, "Error analysis and estimation for the finite volume method with
884 applications to fluid flows," PhD, 1996.

885 [54]H. G. Weller, G. Tabor, H. Jasak, andC. Fureby, "A tensorial approach to
886 computational continuum mechanics using object-oriented techniques," Comput. Phys.
887 **12**, 620 (1998).

888 [55]R. I. Issa, "Solution of the implicitly discretised fluid flow equations by operator-
889 splitting," J. Comput. Phys. **62**, 40 (1986).

890 [56]H. G. Weller, "A new approach to VOF-based interface capturing methods for
891 incompressible and compressible flow," OpenCFD Ltd., Report TR/HGW **4**, 35 (2008).

892 [57]K. J. Vachaparambil, andK. E. Einarsrud, "Comparison of Surface Tension Models
893 for the Volume of Fluid Method," Processes **7**, 542 (2019).

894

895

Accepted to Phys. Fluids 10.1063/5.0127603

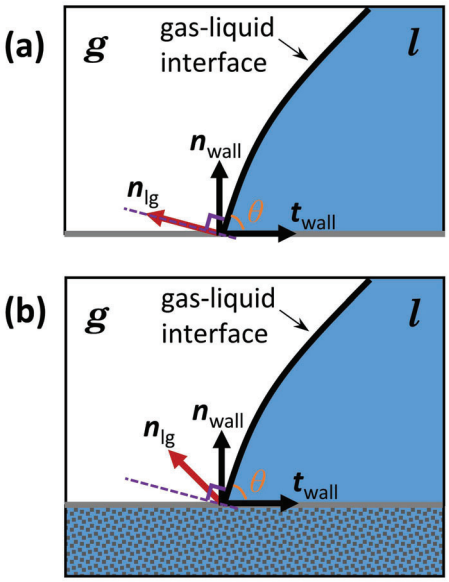

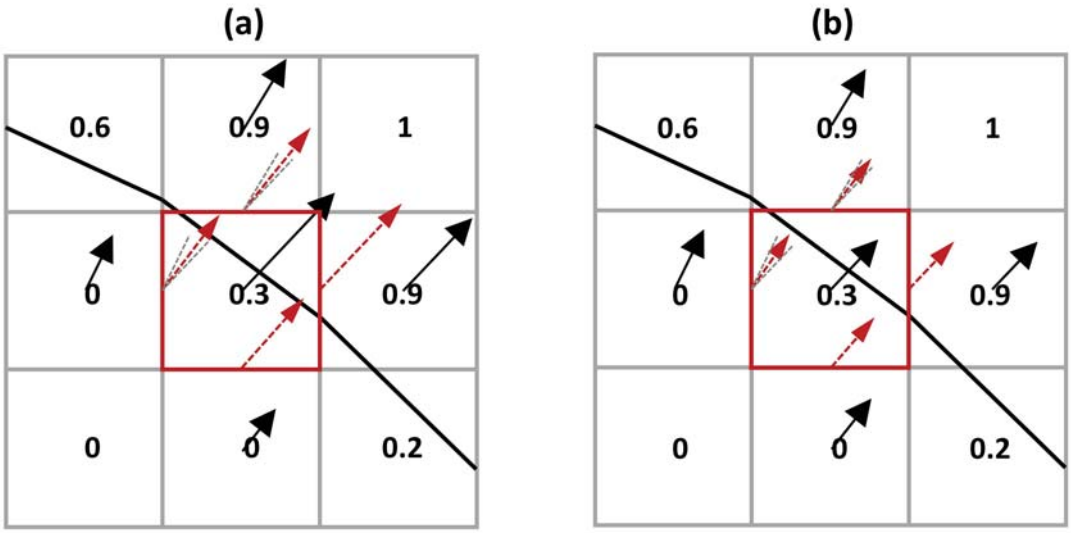

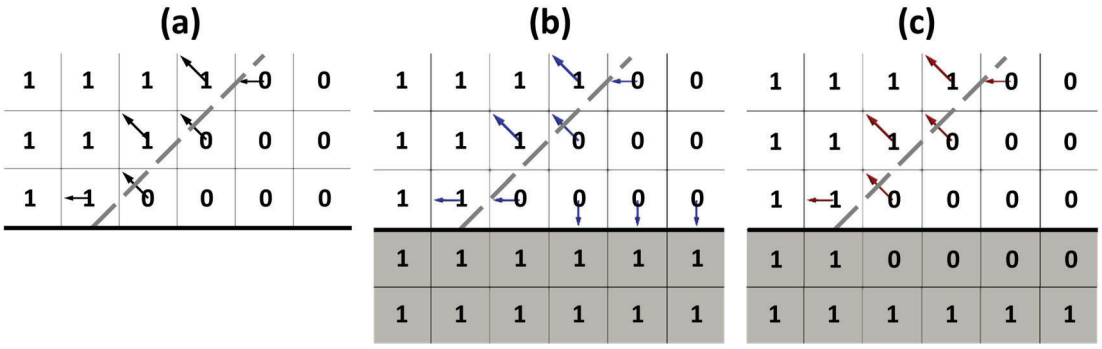

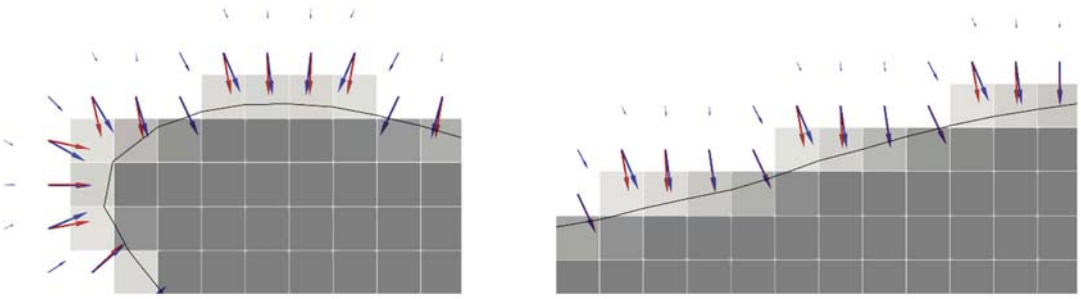

(a) (b)

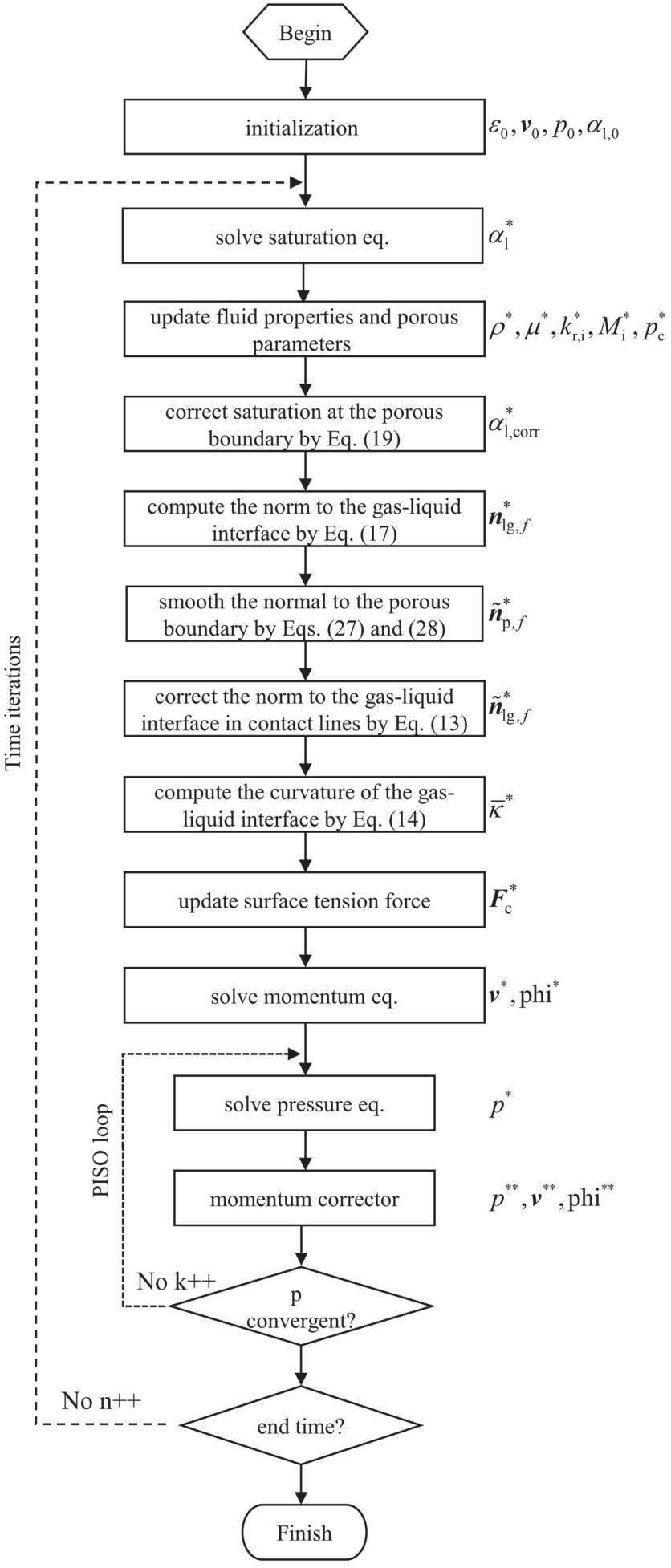

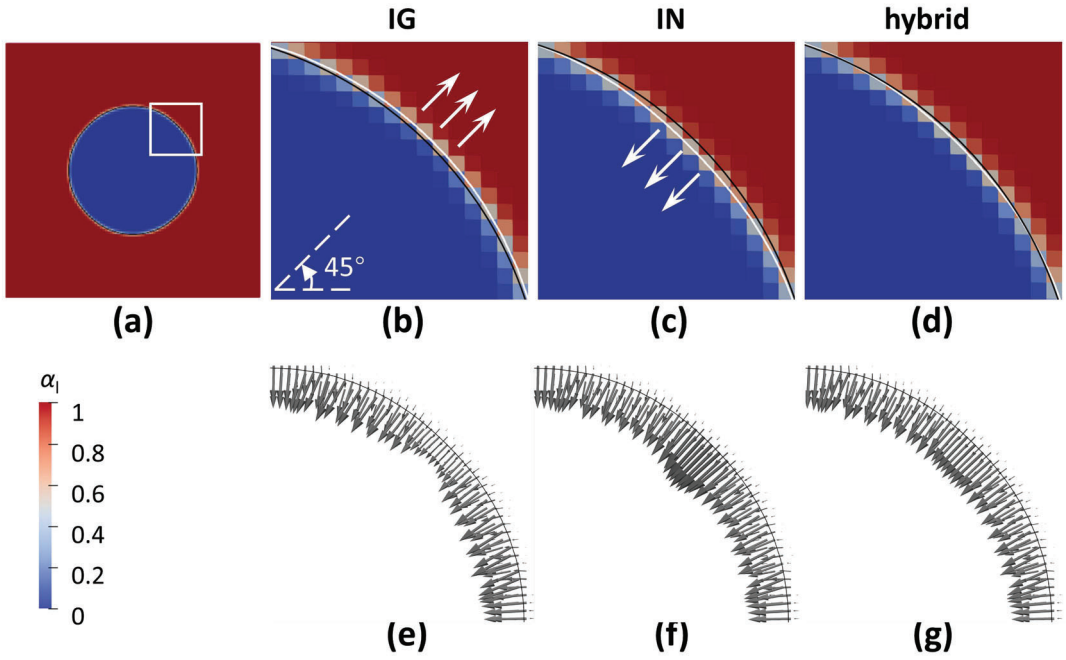

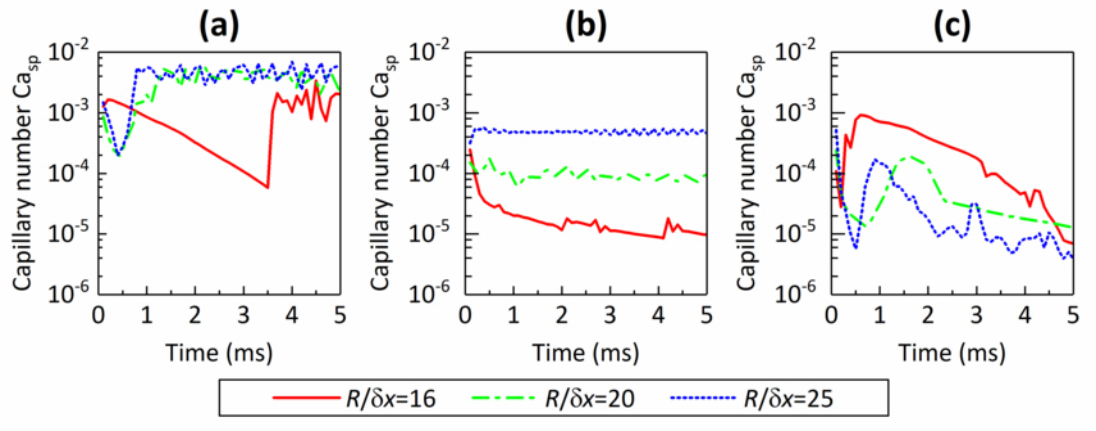
(a)
(b)
(c)
Capillary number Ca_{sp}
10^{-2}
10^{-3}
10^{-4}
10^{-5}
10^{-6}
0 1 2 3 4 5
Time (ms)
$R/\delta x$=16
$R/\delta x$=20
$R/\delta x$=25

Accepted to Phys. Fluids 10.1063/5.0127603

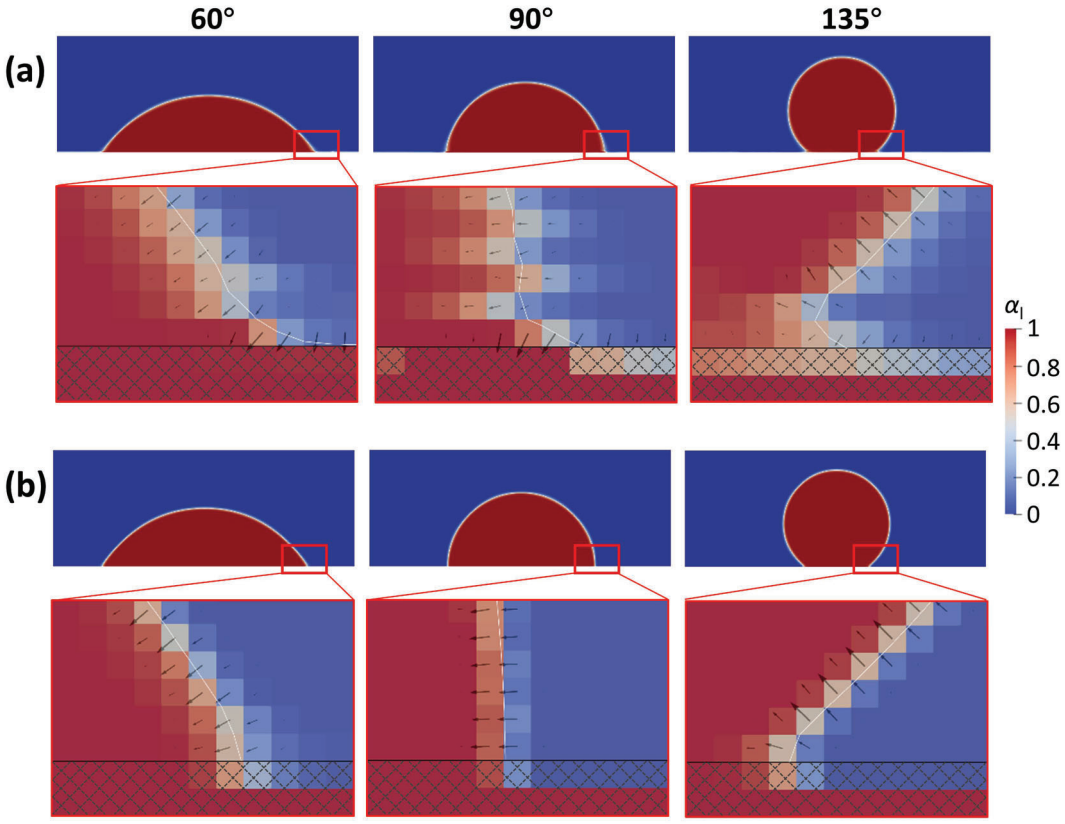

Accepted to Phys. Fluids 10.1063/5.0127603

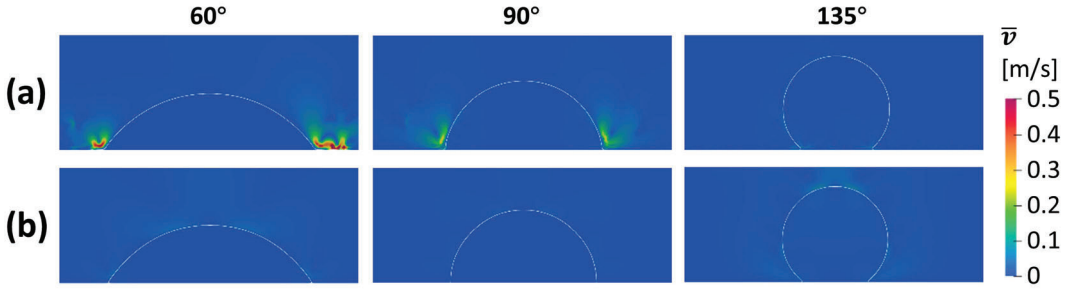

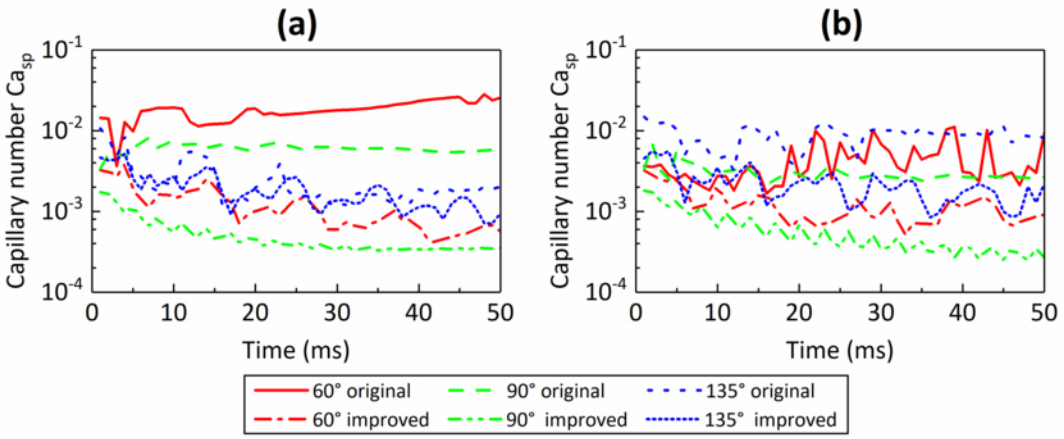
(a)
(b)
Capillary number Ca_{sp}
10^{-1}
10^{-2}
10^{-3}
10^{-4}
0
10
20
30
40
50
Time (ms)
60° original
90° original
135° original
60° improved
90° improved
135° improved

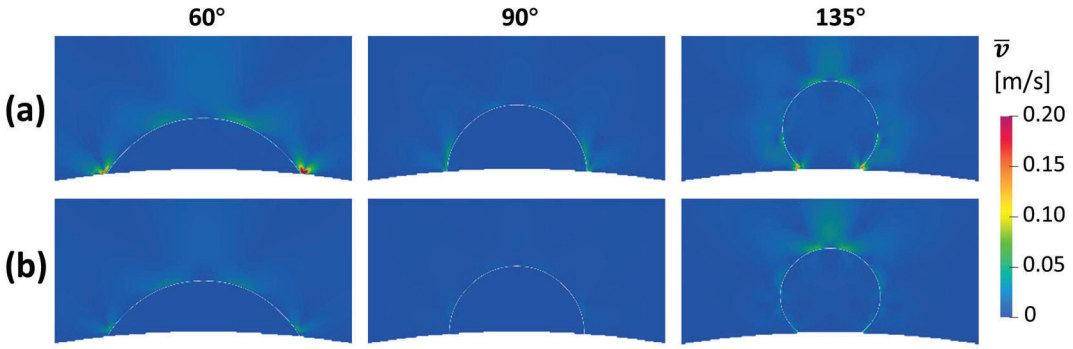

Accepted to Phys. Fluids 10.1063/5.0127603

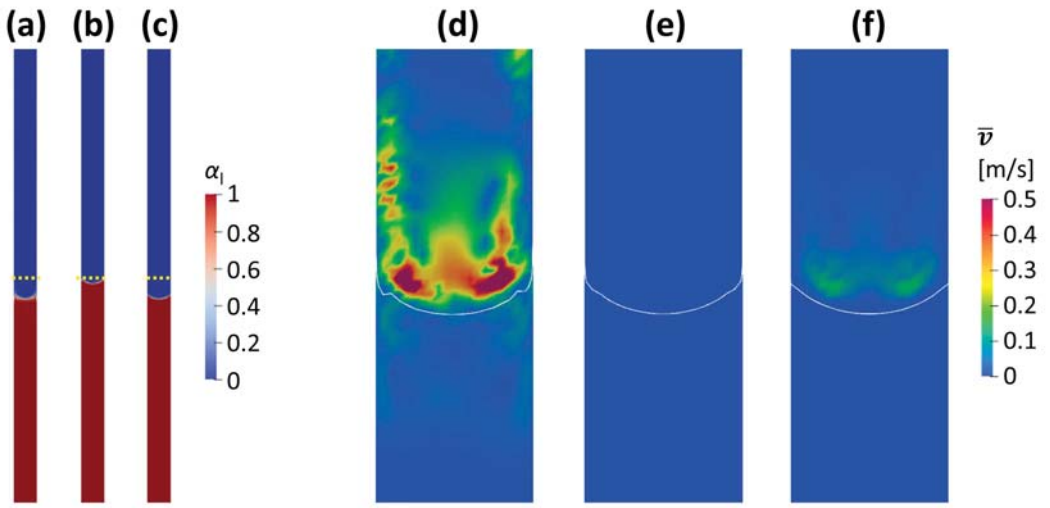

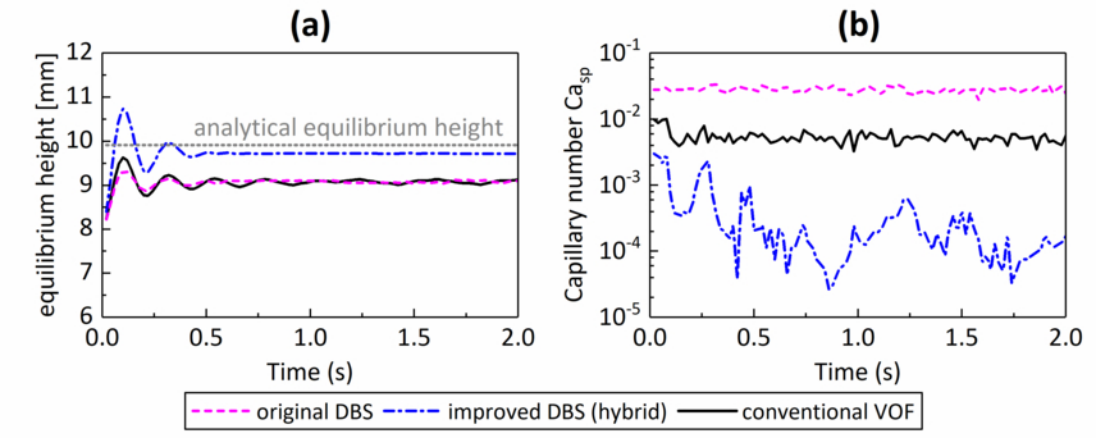
(a)
(b)
equilibrium height [mm]
analytical equilibrium height
Time (s)
Capillary number Ca_{sp}
Time (s)
original DBS
improved DBS (hybrid)
conventional VOF

Accepted to Phys. Fluids 10.1063/5.0127603

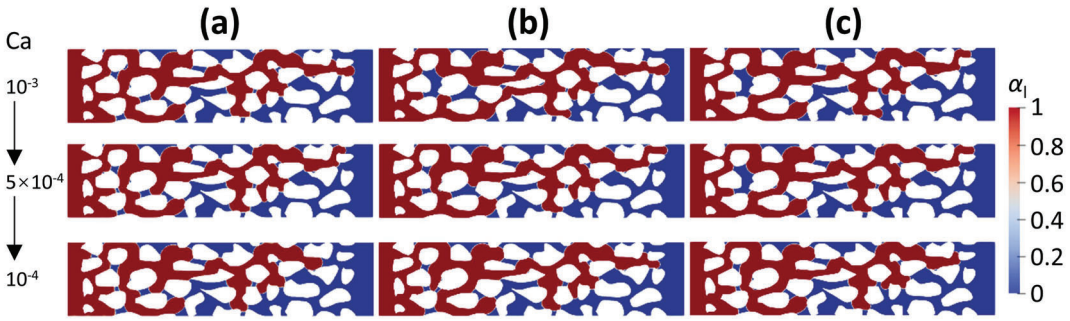

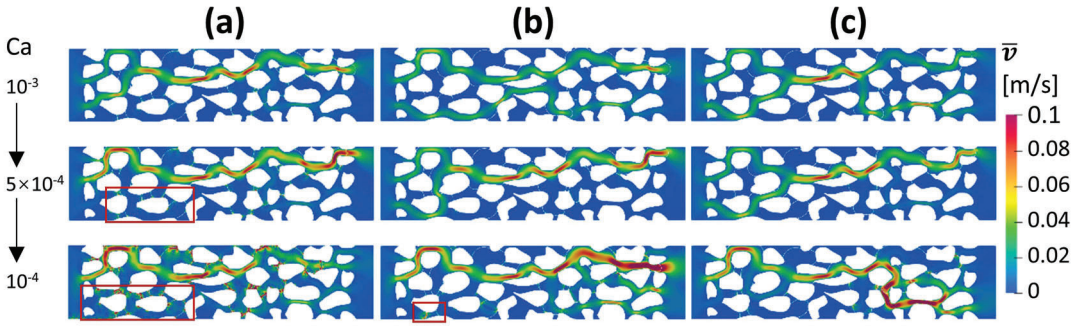

Accepted to Phys. Fluids 10.1063/5.0127603

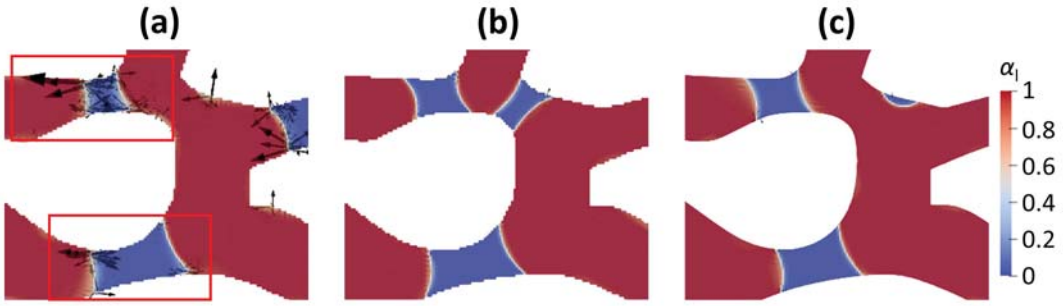

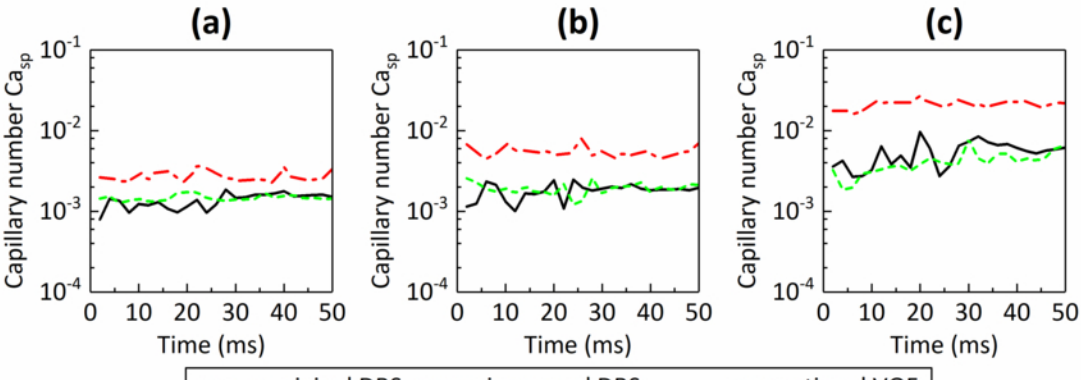
(a)
(b)
(c)
Capillary number Ca_{sp}
10^{-1}
10^{-2}
10^{-3}
10^{-4}
0 10 20 30 40 50
Time (ms)
original DBS
improved DBS
conventional VOF